Activating lattice oxygen based on energy band engineering in oxides for industrial water/saline oxidation

Yijie Zhang[a], Weiyi Zhang[a], Xiaowen Zhang[a], Xin Wang[b], Jiajun Wang[b], Qiang Zhao[a], Yuhan Sun[c,d], Jinping Li[a,c]*, Guang Liu[a]* and Xiaopeng Han[b]*

a Shanxi Key Laboratory of Gas Energy Efficient and Clean Utilization, College of Chemical Engineering and Technology, Taiyuan University of Technology, Taiyuan, Shanxi 030024, P. R. China.

b School of Materials Science and Engineering, Tianjin Key Laboratory of Composite and Functional Materials, Key Laboratory of Advanced Ceramics and Machining Technology (Ministry of Education), Tianjin University, Tianjin300350, P. R. China

c Shanxi Research Institute of HuaiRou Laboratory, Taiyuan, Shanxi 030031, P. R. China.

d 2060 Research Institute, Shanghai Tech University, Shanghai 201210, P. R. China.

*Corresponding author.

E-mail address: jpli211@hotmail.com; liuguang@tyut.edu.cn; xphan@tju.edu.cn

Experimental Section

Chemicals

HCl (1 M), acetone, ethanol, deionized water (>18.2 MΩ), potassium hydroxide (KOH, AR), ammonium fluoride (NH$_4$F, AR), iron(III) chloride hexahydrate (FeCl$_3$·6H$_2$O, AR), urea (CH$_4$N$_2$O, AR), cobalt(II) nitrate hexahydrate (Co(NO$_3$)$_2$·6H$_2$O, AR), ammonium molybdate tetrahydrate ((NH$_4$)$_6$Mo$_7$O$_{24}$·4H$_2$O, AR) and nickel(II) nitrate hexahydrate (Ni(NO$_3$)$_2$·6H$_2$O, AR) were purchased from China National Medicines Corporation Ltd. H$_2^{18}$O (97 atom%) was purchased from Shanghai Aladdin Biochemical Technology Corporation Ltd. All reagents and chemicals were used as received without any further purification.

Preparation of NiMoO on NF and NiO

NiMoO catalyst on NF was synthesized by a one-step hydrothermal method. First of all, Ni foam (NF, thickness: 1.5 mm) was cut into 3 cm*1 cm and purified by sonicated in order of acetone, HCl (1 M), deionized water, and ethanol for 20 min to remove the surface impurities and then dried out in vacuum oven at 80 °C. After that, 1.2 mmol of Ni(NO$_3$)$_2$·6H$_2$O and 0.3 mmol of (NH$_4$)$_6$Mo$_7$O$_{24}$·4H$_2$O were added to deionized water (30 mL) and stirred to form a uniform solution. Then, the PH was adjusted to 5.2 by adding NH$_3$·H$_2$O. Finally, the aqueous solution containing Ni and Mo precursors and a piece of as-prepared NF were transferred to a Teflon-lined stainless-steel autoclave (100 mL), maintained at 150 °C for 6 h to grow hydrate NiMoO$_4$ on Ni foam (denoted as NiMoO).

Preparation of F-NiMoO/FeO and NiMoO/FeO on NF

F-NiMoO/FeO catalyst on NF was synthesized by molten salt method and subsequent dipping method. Firstly, the prepared NiMoO on NF was put into a glass vessel containing 1 g of NH_4F and heated at 120 °C for 50 min. Finally, the precursor was immersed in 0.25 M $FeCl_3$ solutions for 30 s at room temperature and dried at 80 ℃ for 1 h. NiMoO/FeO catalyst on NF was synthesized by the same method, except for fluoridation. Besides, we also explored the influence of different fluorination duration and different dipping concentration.

Preparation of NiO, NiFeO and F-NiFeO on NF

Electrochemical activation of the pre-catalysts was performed by the cyclic voltammetry (CV) scanning in a standard three-electrode electrochemical cell using 1 M KOH solution as electrolyte at 25 °C. The obtained pre-catalyst (work surface area:1 cm*1 cm), Hg/HgO (1 M KOH solution), and graphite rod were severed as the working electrode, reference electrode, and counter electrode, respectively. In all, 20 cycles of CV scanning were conducted for each sample in the potential region from 0.1 to 1.9 V versus Hg/HgO at a sweep rate of 20 mV s^{-1} to achieve in situ reconstruction. The activated NiMoO, NiMoO/FeO and F-NiMoO/FeO were denoted as NiO, NiFeO and F-NiFeO. The catalyst loading was calculated to be ~0.012 g cm^{-2} from weight difference between commercial NF and as prepared F-NiFeO on NF.

Preparation of CoO, CoFeO and F-CoFeO on NF

CoMoO catalyst on NF was synthesized by the same method, except that $Ni(NO_3)_2 \cdot 6H_2O$ is replaced by $Co(NO_3)_2 \cdot 6H_2O$. CoMoO/FeO and F-CoMoO/FeO catalyst on NF were synthesized by the same method, except that NiMoO is replaced

by CoMoO. And the activated CoMoO, CoMoO/FeO and F-CoMoO/FeO were denoted as CoO, CoFeO and F-CoFeO.

Preparation of Ni(OH)$_2$-A, Fe-Ni(OH)$_2$-A, and F, Fe-Ni(OH)$_2$-A on NF

Ni(OH)$_2$ catalyst on NF was synthesized by a one-step hydrothermal method. First of all, 2 mmol of Ni(NO$_3$)$_2$·6H$_2$O, 1 mmol NH$_4$F and 3 mmol CH$_4$N$_2$O were added to deionized water (30 mL) and stirred to form a uniform solution. Then, the aqueous solution and a piece of as-prepared NF were transferred to a Teflon-lined stainless-steel autoclave (100 mL), maintained at 120 °C for 6 h. Finally cool to room temperature, wash and dry to obtain Ni(OH)$_2$. Ni(OH)$_2$/FeO and F-Ni(OH)$_2$/FeO catalyst on NF were synthesized by the same method, except that NiMoO is replaced by Ni(OH)$_2$. And the activated Ni(OH)$_2$, Ni(OH)$_2$/FeO and F- \Ni(OH)$_2$/FeO were denoted as Ni(OH)$_2$-A, Fe-Ni(OH)$_2$-A, and F, Fe-Ni(OH)$_2$-A.

Materials Characterizations

The morphology of the obtained materials was conducted by scanning electron microscopy (SEM, Hitachi SU8010, 3 kV) and transmission electron microscopy (TEM, JEOL 2010FEF, 200 kV). X-ray diffraction (XRD, Bruker D8 Advance, Cu Kα radiation) was used to analyze the crystallinity of the products. The composition was analyzed by Raman spectra (InVia 1WU072, 532 nm) and inductively coupled plasma-optical emission spectroscopy (ICP-OES, Agilent 5110). Samples' wettability was studied using a KRUSS contact angle instrument (DSA100). X-ray photoelectron spectroscopy (XPS) was investigated on a Thermo VG ESCALAB250 to analyze the surface composition and bonding configuration. X-ray absorption spectroscopy (XAS)

measurements were performed using an Easy XES150 system (Easy XAFS LLC, USA) for analyzing the entire chemical state and structure of the catalyst. The Ni K-edge was measured with Si 551 crystal, and air-cooled tube with Pd outputting at 30 kV and 2.5 mA. The soft XAS of Ni L-edge and O K-edge were measured on beamline B12b at the National Synchrotron Radiation Laboratory (NSRL, China) in the total electron yield (TEY) mode by collecting the sample drain current under a vacuum better than 1×10^{-7} Pa. The beam from the bending magnet was monochromatized by utilizing a varied line-spacing plane grating and refocused by a toroidal mirror. The energy range is 100–1000 eV with an energy resolution of ~0.2 eV. Differential electrochemical mass spectrometry (DEMS) measurements were carried out using a QAS 100 device (Linglu Instruments, Shanghai).

Electrochemical measurements

A three-electrode system was conducted to perform all electrochemical measurements under the temperature of 25 °C. The obtained electrocatalyst (work surface area:1 cm*1 cm), Hg/HgO (1 M KOH solution), and graphite rod were severed as the working electrode, reference electrode, and counter electrode, respectively. The measured potentials versus Hg/HgO could be converted to the potentials versus reversible hydrogen electrode (RHE) by Equation (1):

$$E_{RHE} = E_{Hg/HgO} + 0.098 + 0.059 \times PH \qquad (1)$$

Oxygen evolution reaction (OER) was tested in 1 M KOH solution (pH = 13.6) and 1 M KOH with 0.5 M NaCl solution (pH = 13.6). Electrochemical performance was investigated by reverse scan linear sweep voltammetry (RLSV, corrected by the manual

95% iR compensation) curves in the potential region from 1.9 to 0.1 V versus Hg/HgO at a scan rate of 2 mV s^{-1}. The R is obtained from electrochemical impedance spectroscopy (EIS), with the frequency range of 10^5 to 1 Hz and an amplitude of 10 mV. Tafel slopes were obtained by plotting potential against log (j) from RLSV curves. The apparent electrochemical activation energy (E_a) for OER is calculated by using the Arrhenius relationship:

$$\frac{\partial ln(i_0)}{\partial(1/T)} = -\frac{E_a}{R} \qquad (2)$$

where i_0 is the exchange current density, T is the temperature, and R is the gas constant. Specifically, the RLSV curves of catalysts at different temperatures were measured. Then, the corresponding i_0 values were calculated by fitting the Tafel plots (η = blog(j) + a), where log(i_0) = -a/b at η extrapolated to 0. After compiling ln(i_0) against 1/T, the slopes of curves are their apparent E_a for OER. To evaluate the long-term stability and corrosion resistance of the electrocatalyst, chronopotentiometry (CP) was employed in current densities of 1 A cm^{-2} for 100 h. The real O_2 evolution amount with a constant current density of 1 A cm^{-2} in 1 M KOH and 1 M KOH with 0.5 M NaCl for F-NiFeO electrode was carried out by using a water displacement method in gas burette equipment. The theoretical O_2 evolution amount and Faradaic efficiency were determined with the equations of n_t=Q/4F and η_F=n_{exp}/n_t*100%. While n_{exp} and n_t denote as the experimental and theoretical O_2 evolution amounts, F is the Faradaic constant (96485 C mol^{-1}) and Q represents the total charge.

Calculation of electrochemical active surface area (ECSA)

Electrochemical double-layer capacitances (C_{dl}) were determined by a series of cyclic

voltammetry (CV) ranging from 10 to 120 mV s^{-1} in a non-faradic region. C_{dl} was estimated by plotting the $\Delta j/2 = (j_a - j_c)/2$ at 1 or 1.05 V *vs.* RHE against the sweep rates. Electrochemical surface-active area (ECSA) of synthesized electrodes was calculated by Equation (3):

$$ECSA = \frac{C_{dl}}{C_s \times A}$$

(3)

where C_s is the capacitance of an atomically smooth planar surface (0.04 mF cm^{-2} in alkaline media), and A is the electrode area (1 cm^2 for our working electrodes).

Calculation of turnover frequency (TOF)

The true catalytic activity was evaluated by assessing the amount of oxygen gas generated per unit of time as TOF of Ni active sites via CV. Assuming that all surface metallic sites involve in the Faradaic electron transfer, the mole loading of Ni sites in F-NiFeO, NiFeO and NiO was estimated electrochemically by CV scans of Ni peroxidation peak before OER at incrementing scan rates from 2.5 to 15 mV s^{-1} in 1 M KOH. The obtained slope from the linear regression of the recorded oxidation current responses versus scan rate gives the moles of Ni active sites:

$$Slope = \frac{n^2 F^2 A \Gamma_0}{4RT}$$

(4)

where n is the number of electrons transferred during the oxidation of Ni^{2+} to Ni^{3+} (n =1), F is the Faradic constant, A is the geometrical surface area of the electrode, Γ_0 is the surface concentration of Ni active sites (mol cm^{-2}), R is the ideal gas constant, and T is the absolute temperature. The amount of Ni moles (m) on the surface participating in the OER was then obtained from the product of A and Γ_0.

$$m = A \times \Gamma_0$$

(5)

Afterwards, the TOF value based on Ni active sites was derived according to Equation (6):

$$TOF = \frac{jA}{4mF}$$

(6)

where j is the current density (A cm^{-2}) at a fixed overpotential from the polarization

measurement in 1 M KOH, A is the surface area, 4 indicates the four-electron transfer process in OER, F is the Faradic constant, and m represents Ni mole loadings.

^{18}O-labeling experiment

NiO, NiFeO and F-NiFeO were labeled with ^{18}O-isotopes by operated at a constant potential of 1.0 V *vs.* Hg/HgO in KOH with $H_2^{18}O$ as water source for 300 s. Afterward, the ^{18}O-labeled catalysts were rinsed with $H_2^{16}O$ for serval times to remove the remaining $H_2^{18}O$.

DEMS measurements

Differential electrochemical mass spectrometry (DEMS) measurements were carried out using a QAS 100 device (Linglu Instruments, Shanghai). The NiO, NiFeO or F-NiFeO with ^{18}O-labeling on Au foil, a graphite rod and Hg/HgO (1 M KOH) were used as working electrode, counter electrode, and reference electrode, respectively. CV measurement was performed in KOH solution with $H_2^{16}O$ with a scan rate of 5 mV s^{-1}. In the meantime, gas products with different molecular weights were detected in real time by mass spectroscopy.

In-situ Raman spectra measurements

A home-built top-plate electrochemical cell was used for in situ Raman spectra measurements, in which a graphite rod and Hg/HgO (1 M KOH solution) served as counting electrode and reference electrode, respectively. O_2-saturated 1M KOH solution was act as electrolyte to inject into the cell. To monitor the evolution of catalyst samples during OER process, Raman spectrum was collected after a constant potential was applied to the catalyst electrode for 1 min.

Theoretical simulations

The influence of water molecules and interlayer ions on lattice constant information is considered in the bulk phase structure. In the 2*2*3 NiOOH supercell, the roles of H_2O

and K^+ are considered respectively, the structural formula is $12NiOOH \cdot 6H_2O \cdot 3K$, and the lattice constants are a= 5.85 Å, b= 5.08 Å, c= 20.28 Å, $\alpha=\beta=90°$, $\gamma=120°$. In the $2*4*2$ NiO_2 supercell, the roles of H_2O and K^+ are considered respectively. The structural formula is $4NiO_2 \cdot 2H_2O \cdot K$, and the lattice constants are a= 5.59 Å, b= 14.55 Å, c= 14.54 Å, $\alpha=\beta=90°$, $\gamma=120°$. As for the structure of NiFeOOH, because the doping ratio is relatively small, we constructed the structure of $Fe_3Ni_{45}O_{96}H_{48} \cdot 24H_2O \cdot 12K$ by random doping. Since the oxygen vacancies appear with the doping of F, we further randomly doped F and oxygen vacancies to construct $F_2Fe_8Ni_{40}O_{87}H_{48} \cdot 24H_2O \cdot 12K$ structure. The NiOOH(001), NiFeOOH(102) and F-NiFeOOH(102)-terminated surface were chosen as a computational model because the atomic layer are stable and experimentally available NiOOH, NiFeOOH and F-NiFeOOH structure. For the process of deprotonation, we think about all the deprotonation in the bulk phase structure. The $12NiOOH \cdot 6H_2O \cdot 3K$ structure is obtained by deprotonation of all $12NiOO \cdot 6H_2O \cdot 3K$. After all of $Fe_3Ni_{45}O_{96}H_{48} \cdot 24H_2O \cdot 12K$ and $F_2Fe_8Ni_{40}O_{87}H_{48} \cdot 24H_2O \cdot 12K$ are deprotonated, $Fe_3Ni_{45}O_{96} \cdot 24H_2O \cdot 12K$ and $F_2Fe_8Ni_{40}O_{87} \cdot 24H_2O \cdot 12K$ are obtained. Combined with the characterization results, slab models of NiOOH, $NiFeO_2$ and $F-NiFeO_2$ with O_{vac} were used to represent NiO, NiFeO and F-NiFeO in this work. The doping ratios of Fe and F were obtained from EDS analysis.

The Gibbs free energy changes for the water oxidation steps using single-metal-site mechanism (SMSM) and oxygen-vacancy-site mechanism (OVSM) are calculated. The reaction free energy (ΔG) was calculated according to the following formula:

$$\Delta G = \Delta E + \Delta E_{ZPE} - T\Delta S$$

where ΔE is the electronic energy difference, ΔE_{ZPE} is the corrected zero point of energy, ΔS is the entropy change, and T is the system temperature (298.15 K, in this work).

Calculation details

We have employed the Vienna Ab Initio Package (VASP) to perform all spin-polarized density functional theory (DFT) calculations within the generalized gradient approximation (GGA) using the Perdew-Burke-Ernzerhof (PBE) formulation. We have chosen the projected augmented wave (PAW) potentials to describe the ionic cores and take valence electrons into account using a plane wave basis set with a kinetic energy cutoff of 450 eV. The electronic energy was considered self-consistent when the energy change was smaller than 10^{-5} eV. A geometry optimization was considered convergent when the energy change was smaller than 0.02 eV $\mathrm{\mathring{A}}^{-1}$. The vacuum spacing in a direction perpendicular to the plane of the structure is 18 Å. The weak interaction was described by DFT+D3 method using empirical correction in Grimme's scheme. The COHP of considered atomic pairs was calculated by the Lobster code. The LHB was determined by the 3d-orbital distribution below E_f in DOS diagrams, while the UHB was determined by the unoccupied 3d-orbitals distribution above E_f.
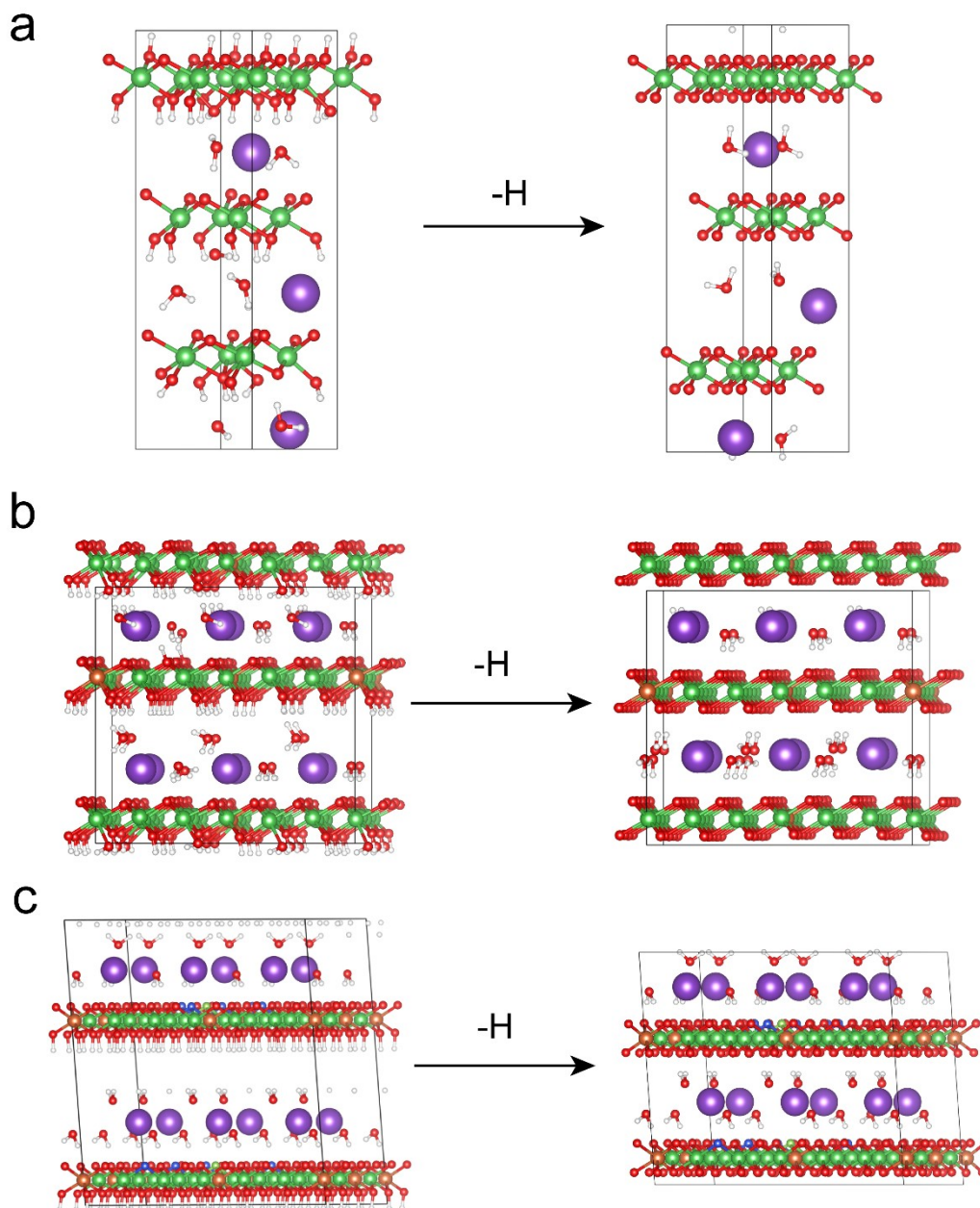
Fig. S1. Schematic diagram of the configuration of (a) NiOOH, (b) NiFeOOH and (c)F-NiFeOOH with O_{vac} and deprotonation of Ni species to form NiO_2, $NiFeO_2$ and F-$NiFeO_2$. (Ni, Fe, O, K, F, H and O_{vac} are shown in green, yellow, red, purple, light green, white and blue, respectively)
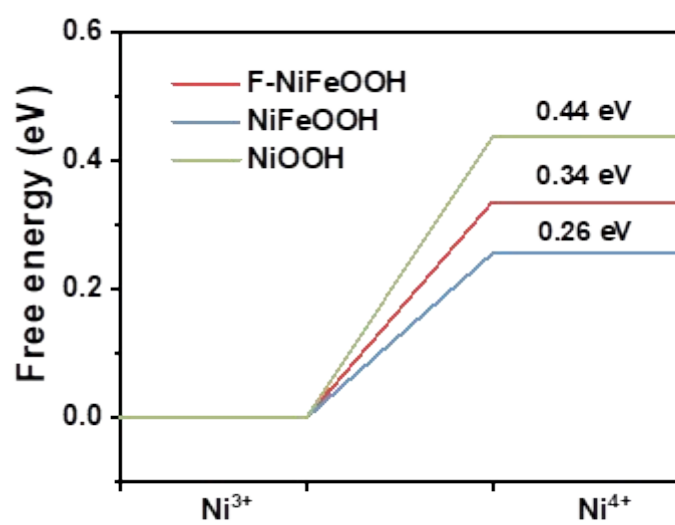
Fig. S2. Free energy diagrams of Ni-species deprotonation.

Table S1. The LHB, UHB and O-2p band center based on the DFT calculation results and integrated COHP of NiOOH, $NiFeO_2$ and $F-NiFeO_2$.

	LHB (eV)	UHB (eV)	O-2p (eV)	ICOPH (eV)
NiOOH	-2.10	1.59	-3.34	-2.67
$NiFeO_2$	-3.34	1.24	-2.41	-2.42
$F-NiFeO_2$	-3.42	1.29	-2.09	-2.20

Table S2. Calculation results of charge transfer energy (Δ) and d-d Coulomb interaction (U) of NiOOH, NiFeO$_2$ and F-NiFeO$_2$.

	Ni-3d (eV)	Δ (eV)	U (eV)
NiOOH	-1.13	2.21	3.69
NiFeO$_2$	-2.46	-0.05	4.58
F-NiFeO$_2$	-2.38	-0.29	4.71
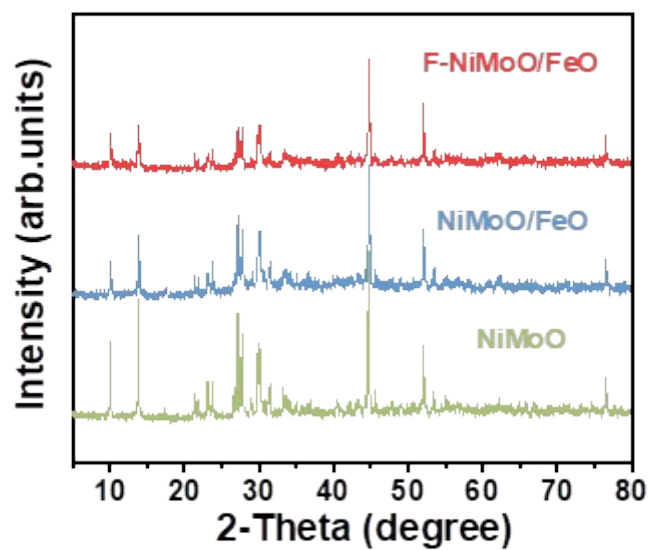
Fig. S3. XRD patterns of NiMoO, NiMoO/FeO and F-NiMoO/FeO. It should be clarified that the three diffraction peaks at 44.45°, 51.27°, and 76.36° match well with the standard card of metallic Ni (PDF#No. 04-0850).
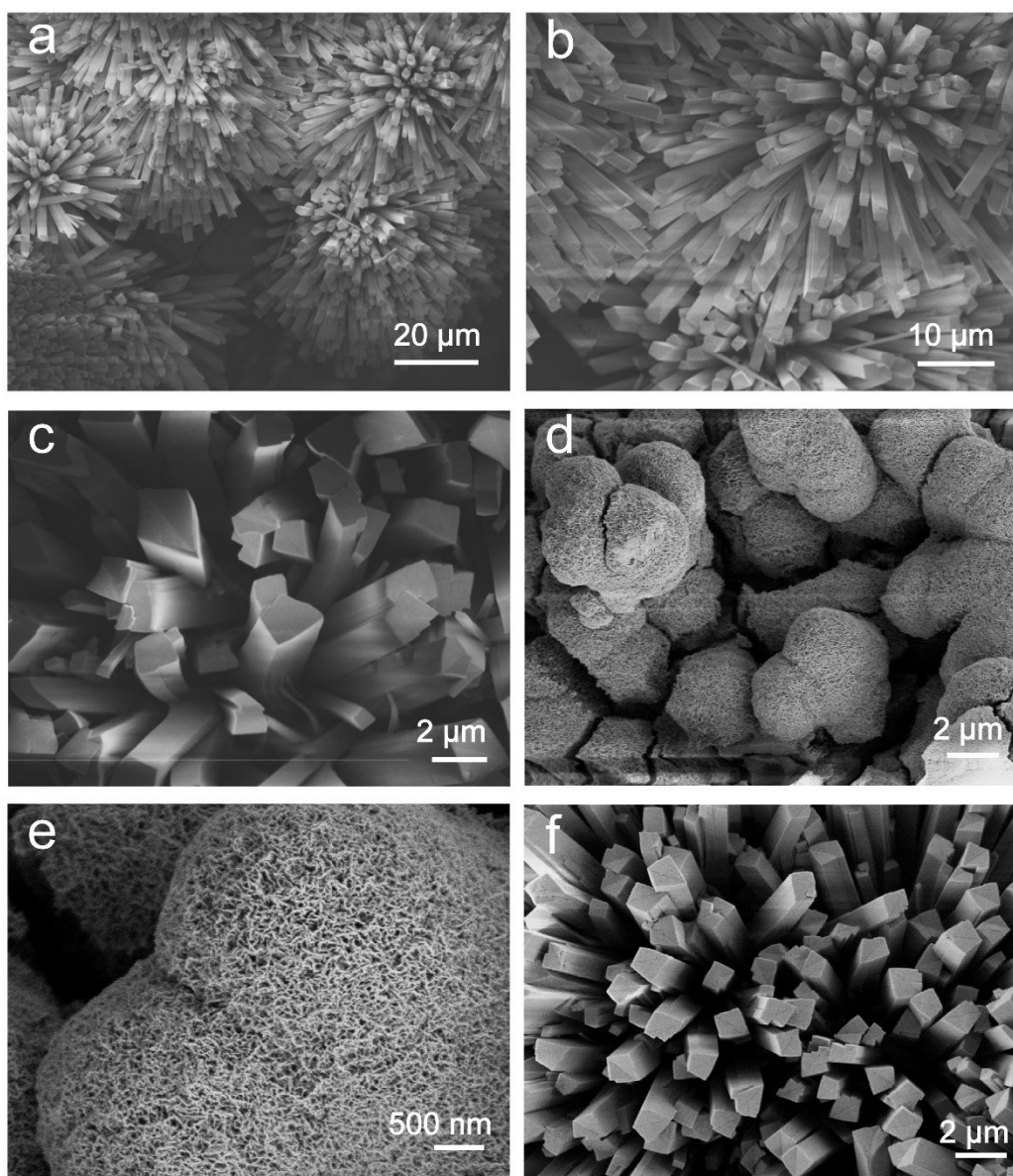
Fig. S4. Low and high magnification SEM images of (**a-c**) NiMoO, (**d-e**) F-NiMoO/FeO and (f) NiMoO/FeO.

16
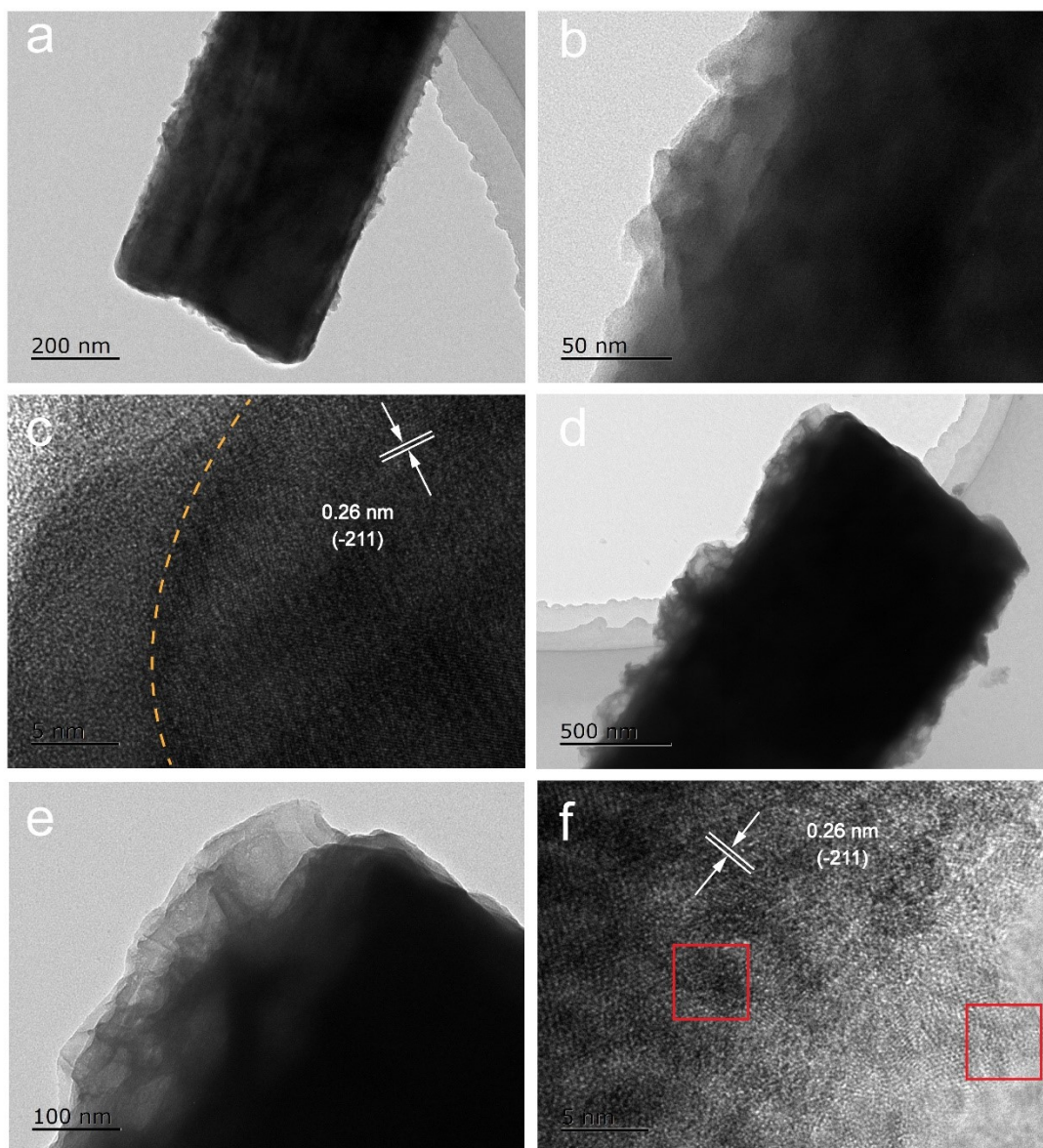
Fig. S5. TEM and HRTEM images of (**a-c**) NiMoO/FeO (the yellow dashed line in Fig. S5c indicates the interface) and (**d-f**) F-NiMoO/FeO (the red boxes in Fig. S5f indicate the presence of lattice defects).
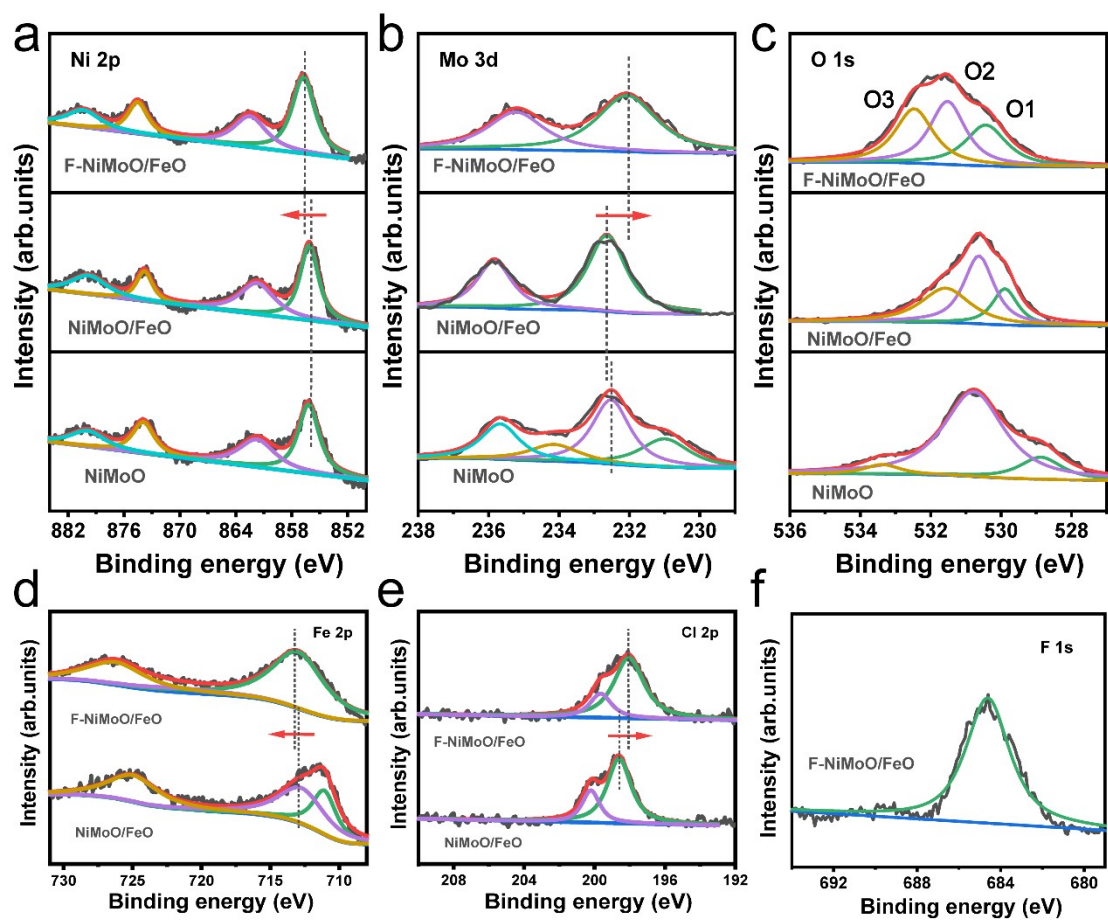
Fig. S6. (**a**) Ni 2p, (**b**) Mo 3d, (**c**) O 1s, (**d**) Fe 2p, (**e**) Cl 2p and (**f**) F 1s XPS spectra of pre-catalysts.
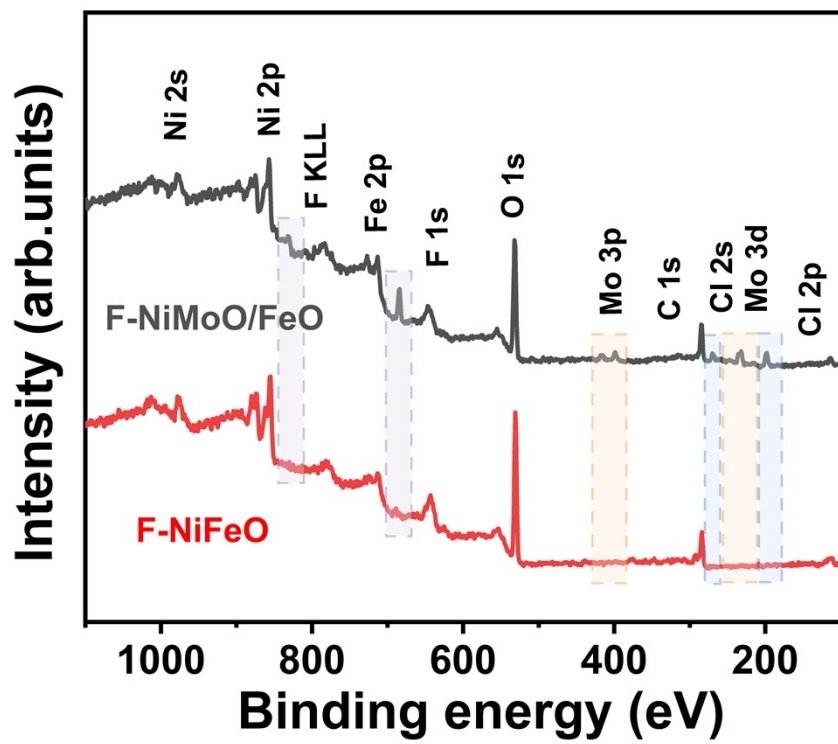
Fig. S7. XPS survey spectra of F-NiMoO/FeO and F-NiFeO.
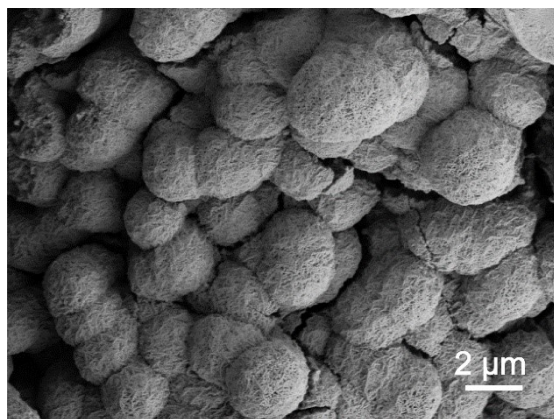
Fig. S8. Low magnification SEM image of F-NiFeO.
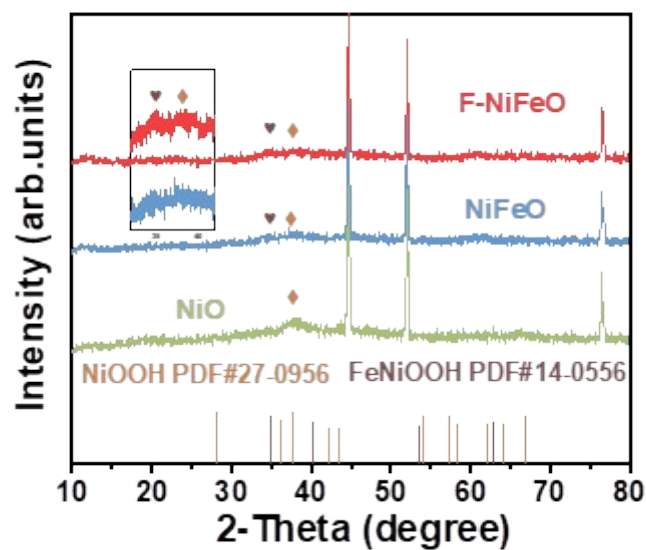
Fig. S9. XRD patterns of NiO, NiFeO and F-NiFeO (the inset is the magnified XRD pattern). The main diffraction peaks at 44.45°, 51.27°, and 76.36° match well with the standard card of metallic Ni (PDF#No. 04-0850). The presence of other weak peaks demonstrates that the NiOOH and FeNiOOH exist in the form of low crystalline structure.
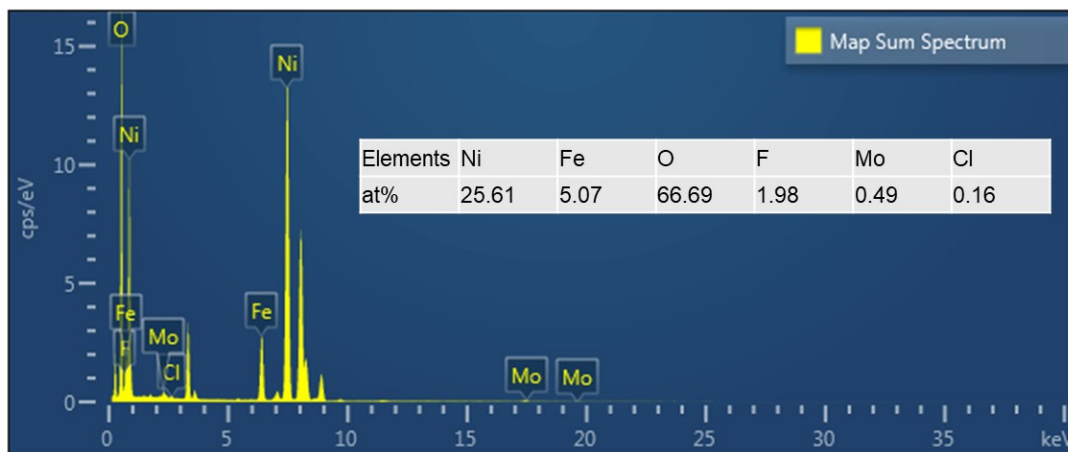
Fig. S10. EDS spectrum of F-NiFeO. Note that the peaks at the 8-10 keV range are attributed to the Cu mesh used for TEM testing.
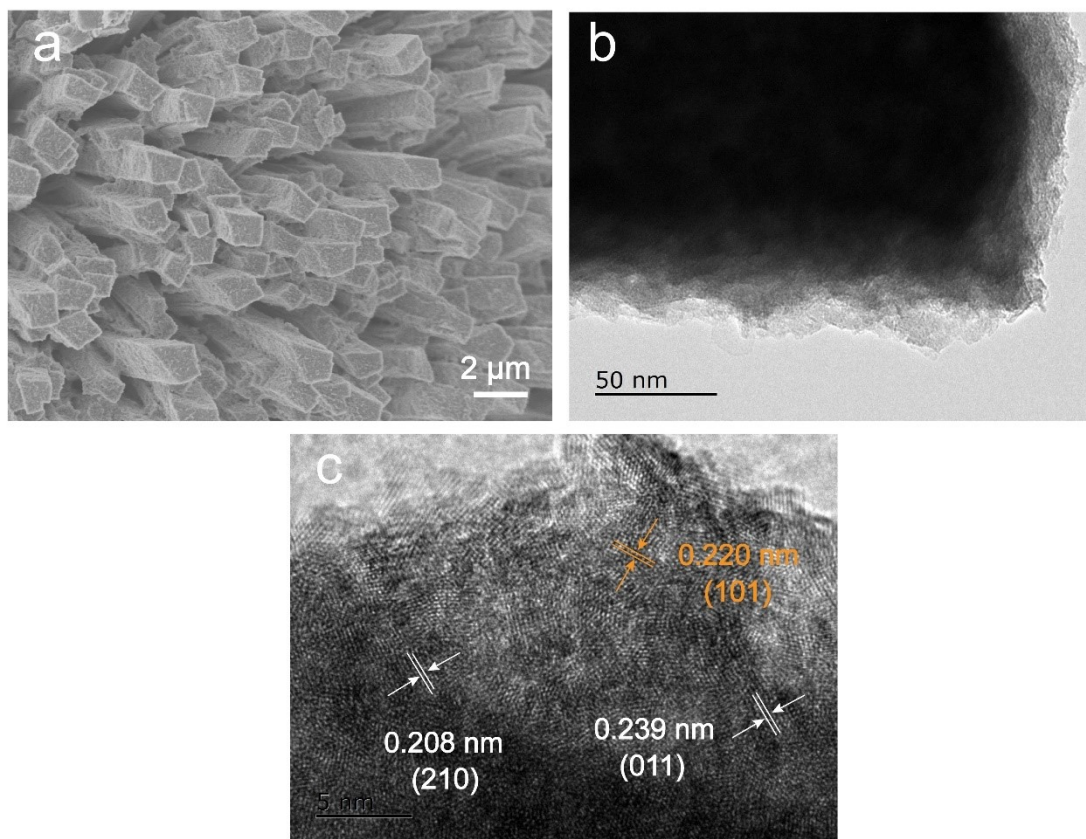
Fig. S11. (**a**) SEM image, (**b**) TEM image and (**c**) HRTEM image of NiFeO.
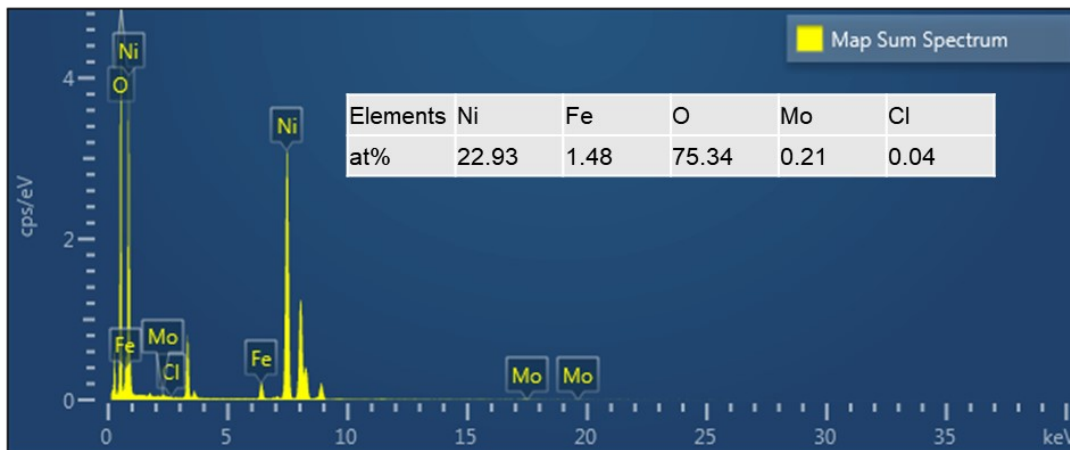
Fig. S12. EDS spectrum of NiFeO. Note that the peaks at the 8-10 keV range are attributed to the Cu mesh used for TEM testing.
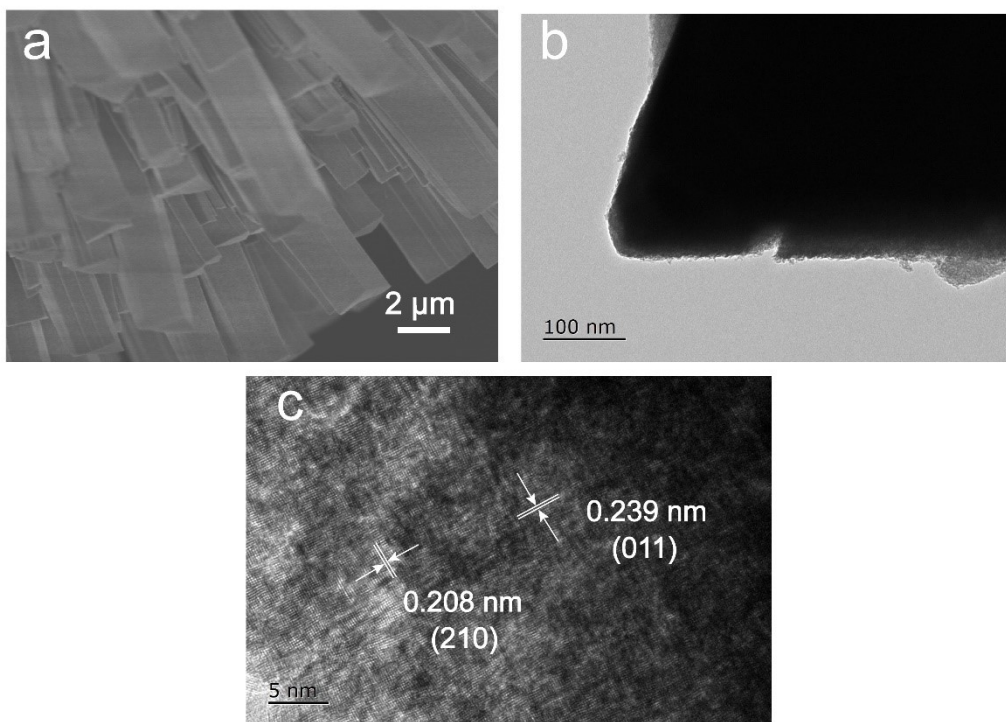
Fig. S13. (**a**) SEM image, (**b**) TEM image and (**c**) HRTEM image of NiO.

Table S3. Elemental composition and atomic ratio detected by ICP.

Atomic (%)	Ni	Fe	Mo
NiO	99.80	/	0.20
NiFeO	97.84	1.94	0.22
F-NiFeO	94.37	5.33	0.30
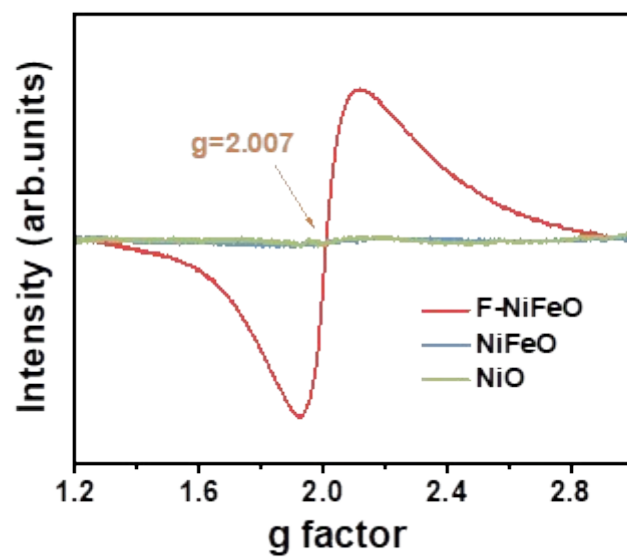
Fig. S14. EPR curves of NiO, NiFeO and F-NiFeO.
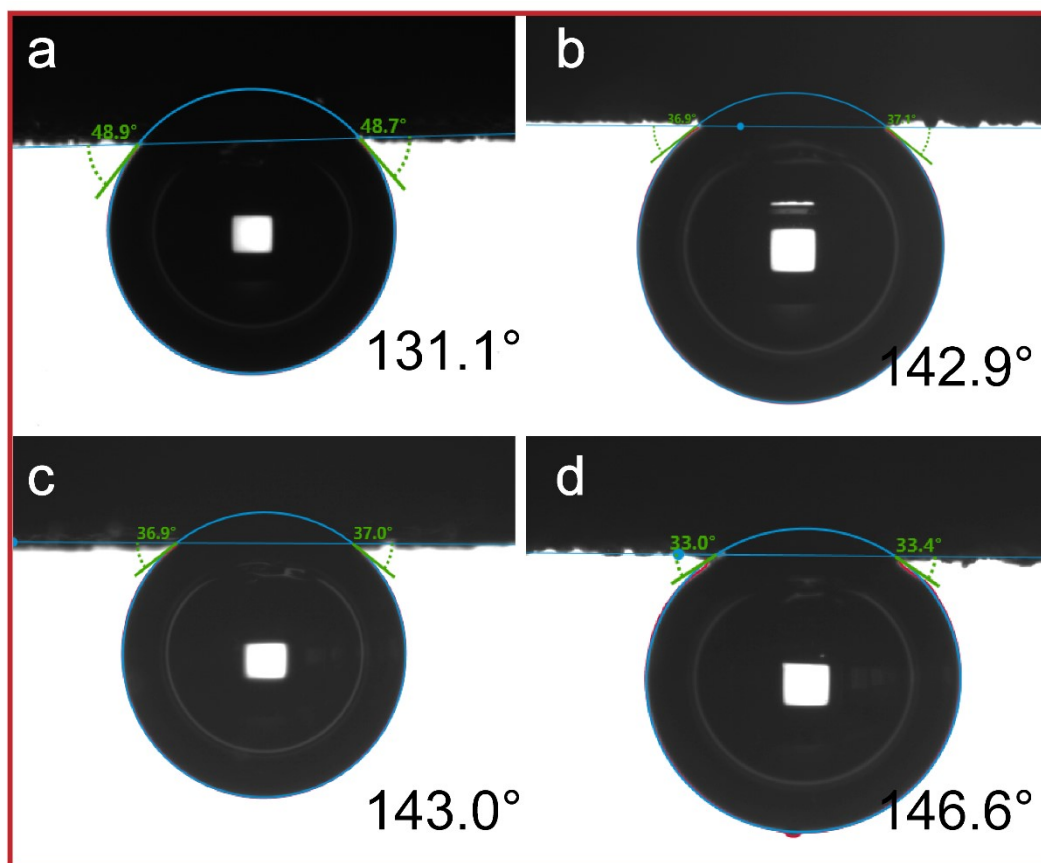
Fig. S15. Contact angle images of (**a**) NF, (**b**) NiO, (**c**) NiFeO and (**d**) F-NiFeO.
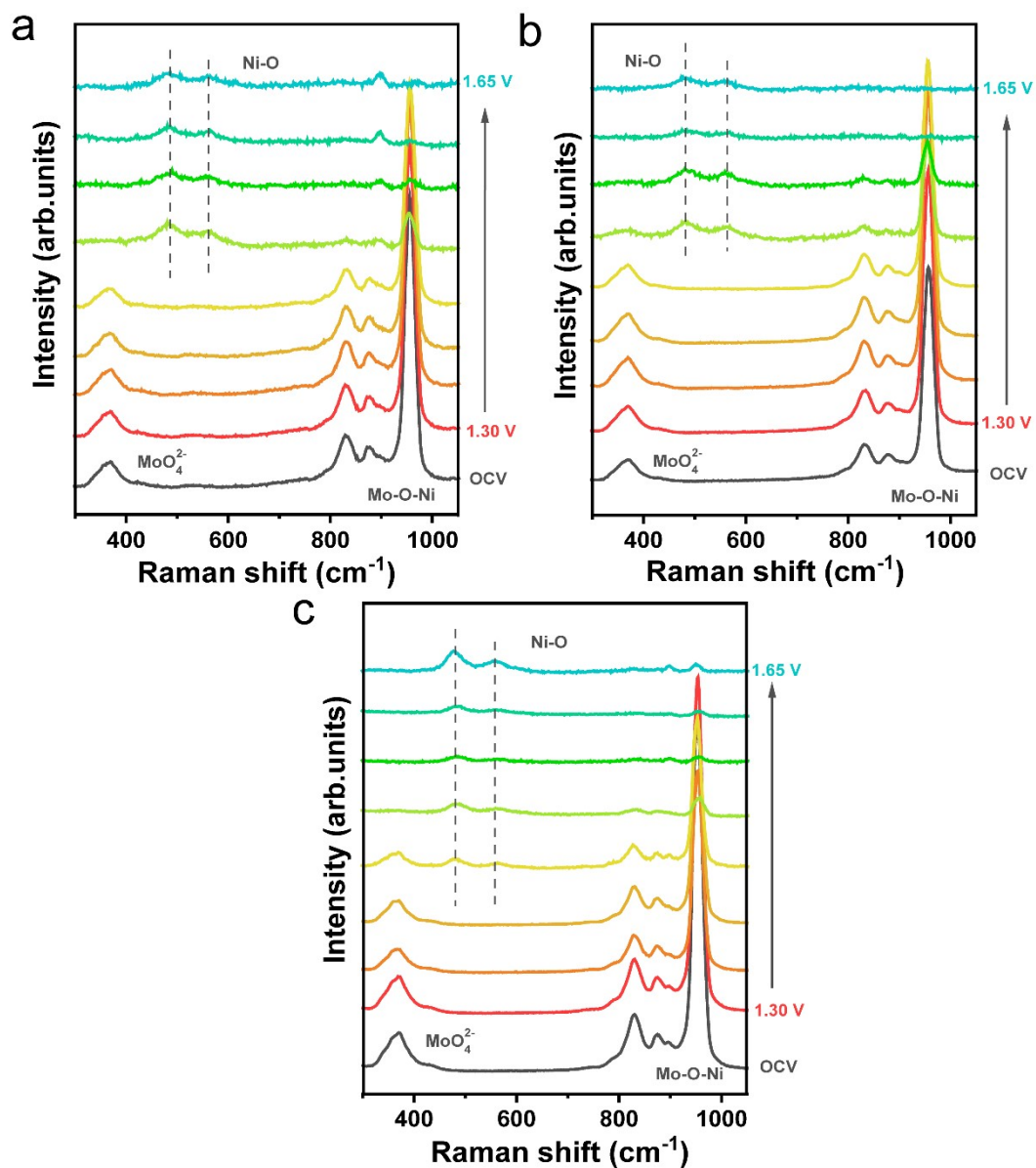
Fig. S16. In-situ Raman spectra of (**a**) F-NiMoO/FeO, (**b**) NiMoO/FeO and (**c**) NiMoO at the operated potentials from 1.3 to 1.65 V vs. RHE. (Raman peak at 897 cm^{-1} corresponds to dissolved MoO_4^{2-} in KOH.)
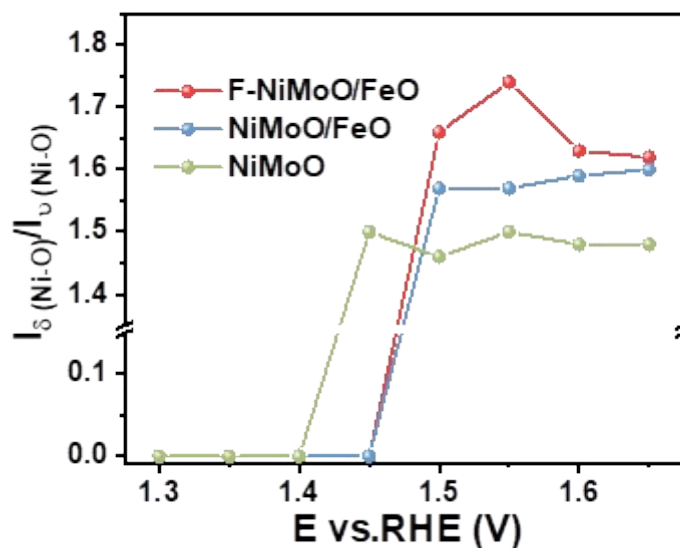
Fig. S17. I_δ/I_ν in the in-situ Raman spectra of F-NiMoO/FeO, NiMoO/FeO and NiMoO. Taking into account the influence of peak intensity and half-peak width, we integrate the peaks at 475 and 549 cm^{-1}, and compare the change of peak area ratio during in-situ Raman process. The results show that F-NiFeO and NiFeO can directly reach a higher integral ratio (I_δ/I_ν) at a higher potential, which proves that Ni^{4+} is generated at 1.5 V.
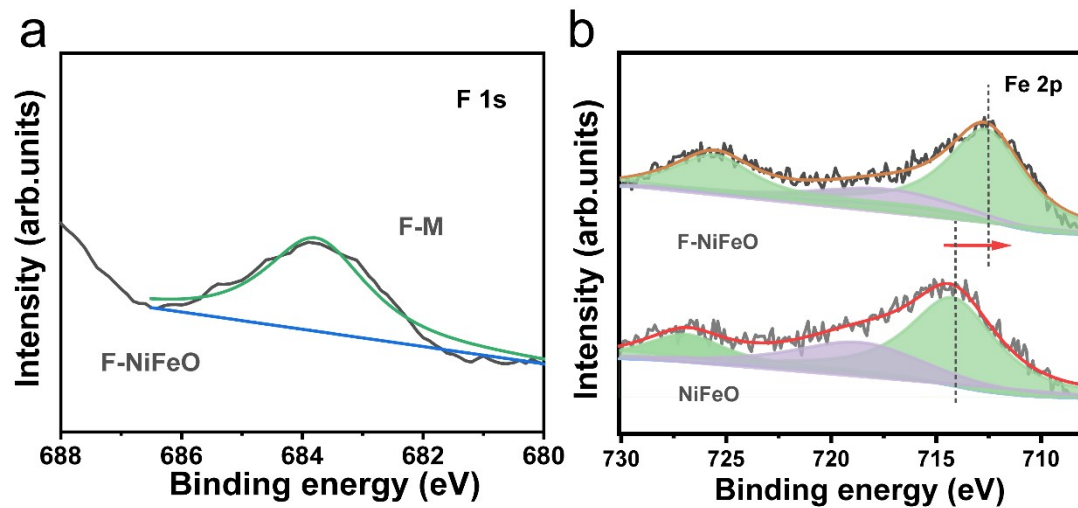
Fig. S18. (**a**) F 1s and (**b**) Fe 2p XPS spectra of prepared catalysts.

Table S4. Quantitative analysis of different oxygen species of NiO, NiFeO and F-NiFeO based on the fitting result of O 1s XPS spectra in Fig. 3b.

(%)	O1	O2	O3
NiO	21.27	55.89	22.84
NiFeO	36.17	36.39	27.44
F-NiFeO	25.73	40.27	34.00

NiO Ni^{3+}

e$_g$ ↑ ↑

t$_{2g}$ ↑↓ ↑↓ ↑

Ni^{2+}

e$_g$ ↑ ↑

t$_{2g}$ ↑↓ ↑↓ ↑↓

NiFeO Ni^{4+}

e$_g$ ↑ —

t$_{2g}$ ↑↓ ↑↓ ↑

F-NiFeO Ni^{4+}

e$_g$ ↑ ↑

t$_{2g}$ ↑↓ ↑↓ ↑
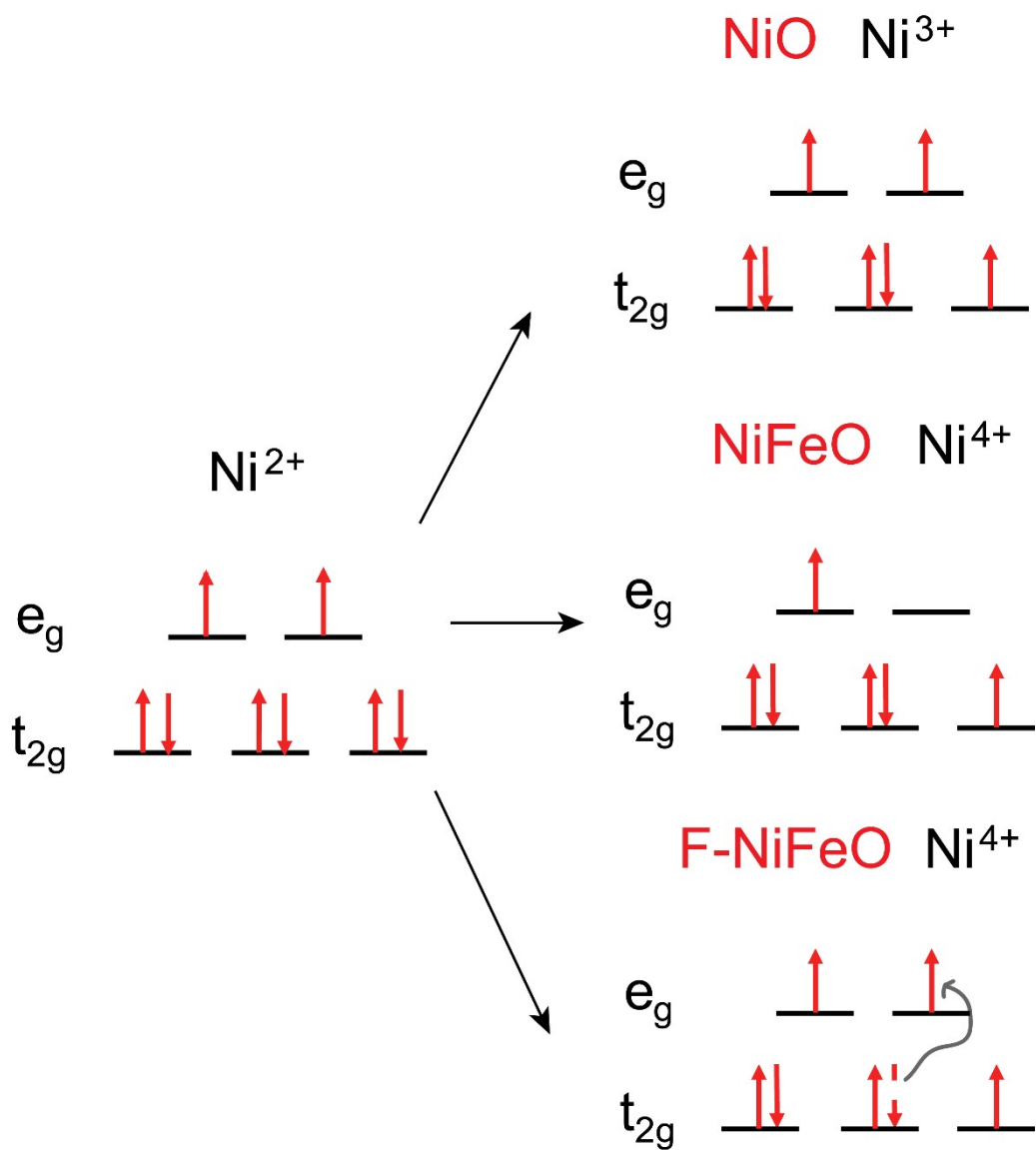
Fig. S19. Schematic illustration of the variation of electron configuration.
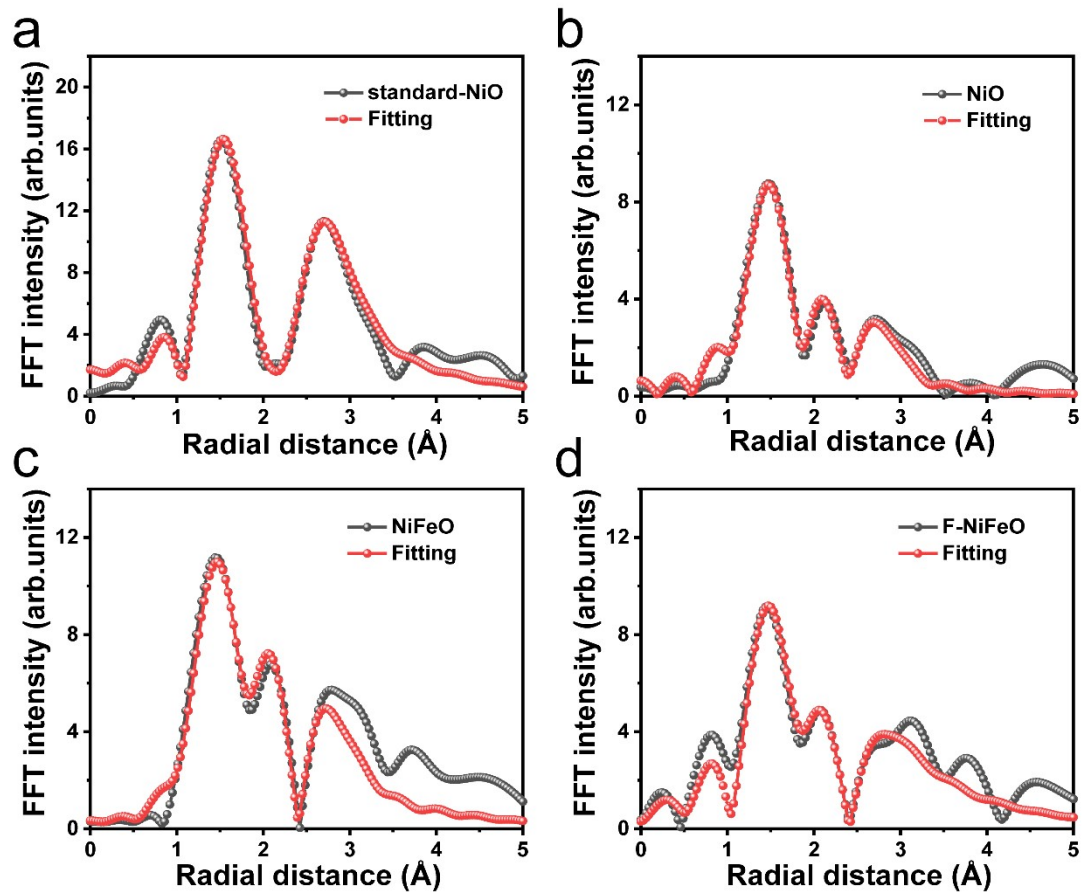
Fig. S20. EXAFS of (**a**) standard-NiO, (**b**) NiO, (**c**) NiFeO and (**d**) F-NiFeO.

Table S5. Structural parameters for EXAFS fits of standard-NiO, NiO, NiFeO and F-NiFeO (S_0^2=0.70).

Sample	Path	N	$\triangle E$ (eV)	R (Å)	σ^2 (Å^2)
standard-NiO	Ni-O	6.0	-4.71	2.04	0.003
	Ni-Ni	6.0		3.09	0.001
NiO	Ni-O	6.0	-6.82	1.97	0.004
	Ni-Ni	4.2		2.76	0.007
	Ni-Ni	1.8		2.96	0.009
NiFeO	Ni-O	4.5	-6.33	1.90	0.003
	Ni-O	1.5		2.05	0.005
	Ni-Ni	4.2		2.79	0.002
	Ni-Ni/Fe	1.5		2.99	0.007
F-NiFeO	Ni-O/F	2.8	-4.55	1.88	0.010
	Ni-O	2.9		1.97	0.004
	Ni-Ni	3.5		2.77	0.002
	Ni-Ni/Fe	2.0		2.98	0.010
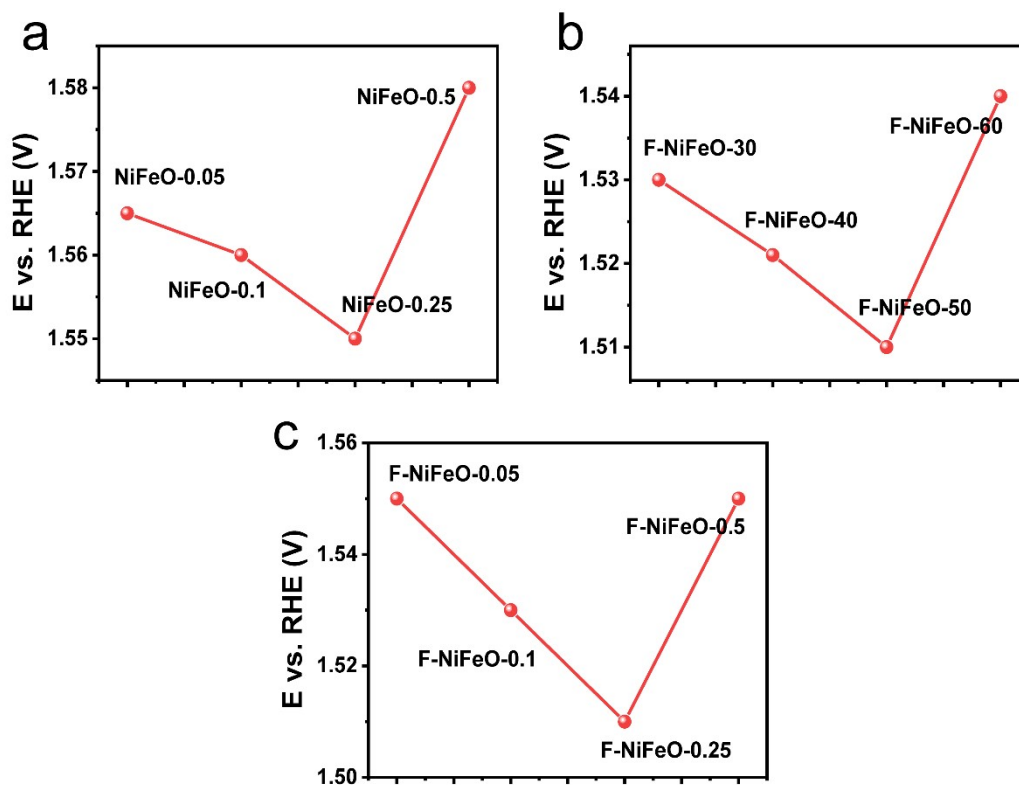
Fig. S21. Potentials of different (**a**) concentration of FeCl₃ solution of NiFeO (denoted as NiFeO-X, X is concentration of FeCl₃ solution), (**b**) duration of molten salt treatment (denoted as F-NiFeO-Y, Y duration of molten salt treatment) and (**c**) concentration of FeCl₃ solution of F-NiFeO (denoted as F-NiFeO-X, X is concentration of FeCl₃ solution) at 1 A cm⁻².
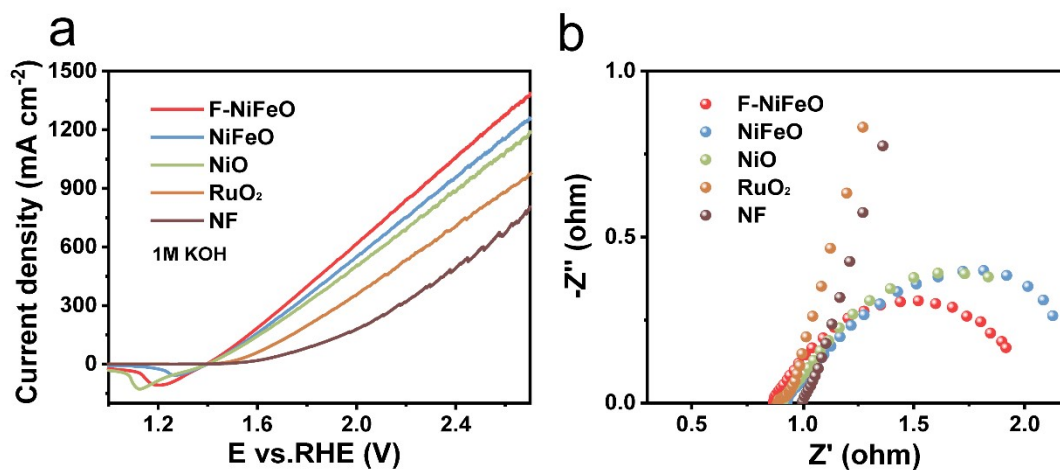
Fig. S22. (**a**) RLSV curves without iR-compensation and (**b**) Nyquist plots of the electrodes in 1 M KOH. Considering the high load of F-NiFeO (0.012 g cm^{-2}) and the deep oxidation of Ni, a large number of accessible active sites are generated, resulting in a large reduction peak.
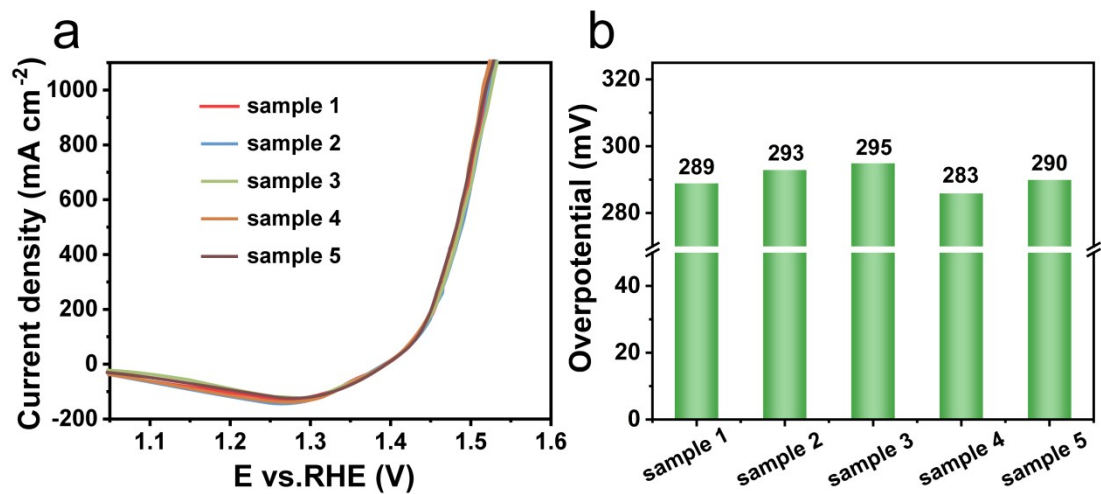
Fig. S23. (**a**) RLSV curves with iR-compensation and (**b**) overpotentials at 1 A cm^{-2} of F-NiFeO samples from different batches.
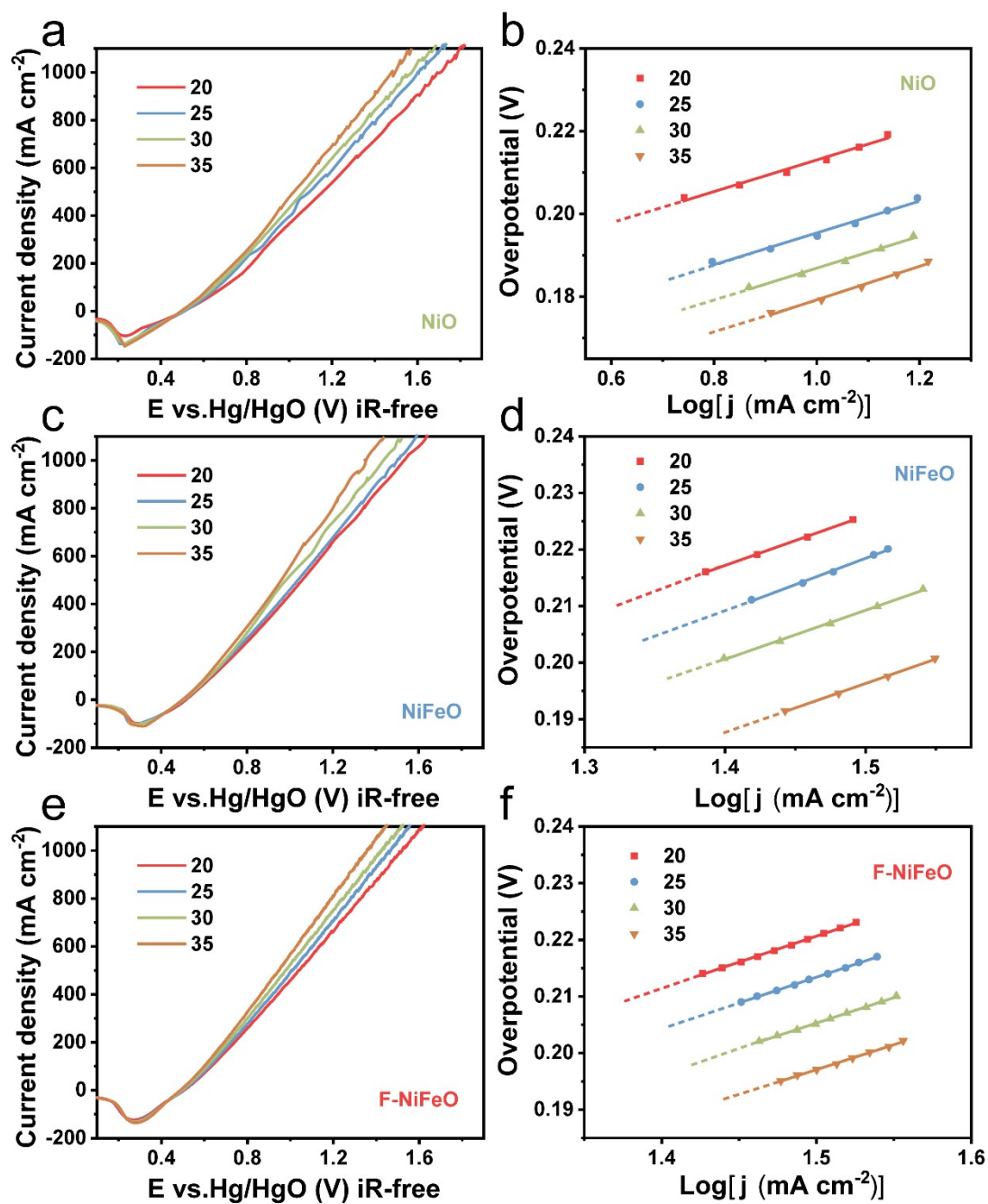
Fig. S24. RLSV curves without iR-compensation at 20 °C, 25 °C, 30 °C and 35 °C, respectively and corresponding Tafel plots as a function of temperature for NiO, NiFeO and F-NiFeO.
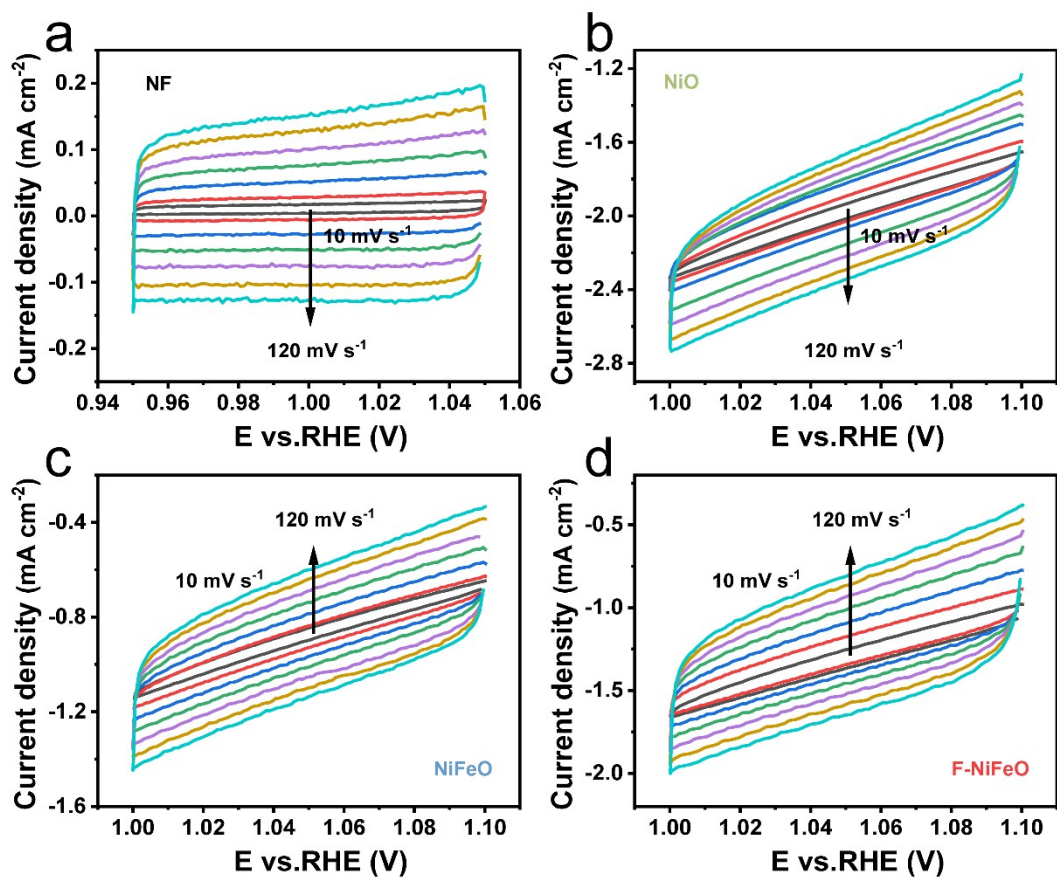
**Fig. S25**. CV scans of (**a**) NF, (**b**) NiO, (**c**) NiFeO and (**d**) F-NiFeO.
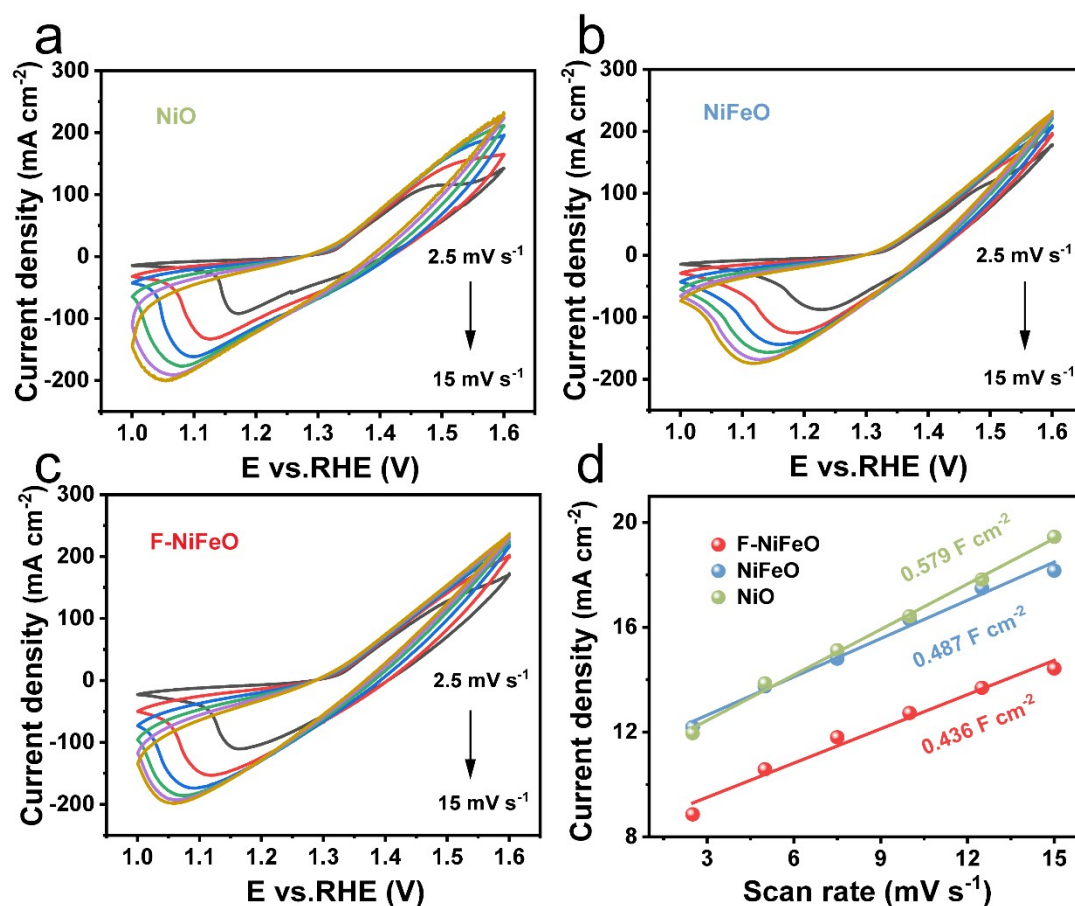
Fig. S26. CV scans of Ni redox of (**a**) NiO, (**b**) NiFeO and (**c**) F-NiFeO. (**d**) the corresponding anodic charging currents as a function of scan rate. Due to the influence of mass transfer diffusion control during OER and the OER polarization current, the oxidation peak and reduction peak of Ni are not completely symmetric, but a quasi-reversible process. In addition, the CV scanning voltage range and sample starting state used for TOF calculation (0.1 - 0.7 V vs. Hg/HgO) are different from RLSV scanning (1.9 - 0.1 V vs. Hg/HgO), resulting in inconsistent reduction peaks for different tests of F-NiFeO.

41

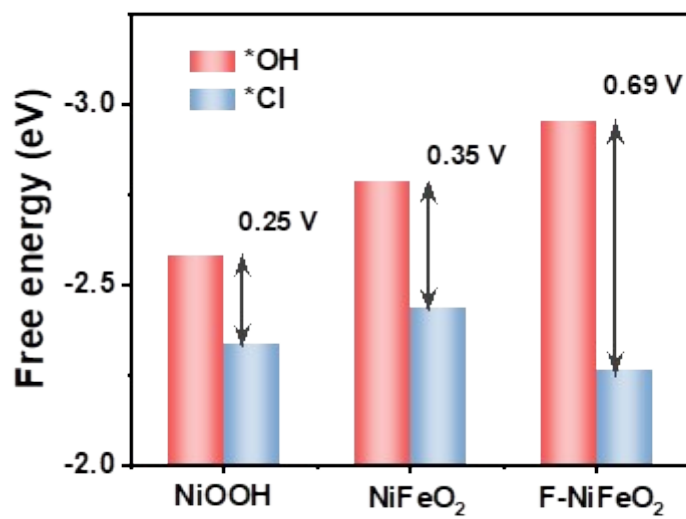**Table S6.** TOF comparisons with the most of recently reported transition metal based electrocatalysts.

Catalysts	TOF (s^{-1})	E (V)	Ref.
F-NiFeO	**3.86**		**This work**
NiFeO	**2.22**	**1.50**	
NiO	**0.97**		
$Cu_2S/CoFeCuOOH$	3.20	1.53	[1]
NiFe LDH-PMo12	2.03	1.58	[2]
EA-FCCN	0.483	1.53	[3]
$FeNi(MoO_4)_x$	0.17	1.506	[4]
FePB/NiFeP	1.50	1.50	[5]
F-NiFe-A	0.25	1.53	[6]
S-FeOOH/IF	1.20	1.50	[7]
FeOOH/NiFe LDH	4.61	1.53	[8]
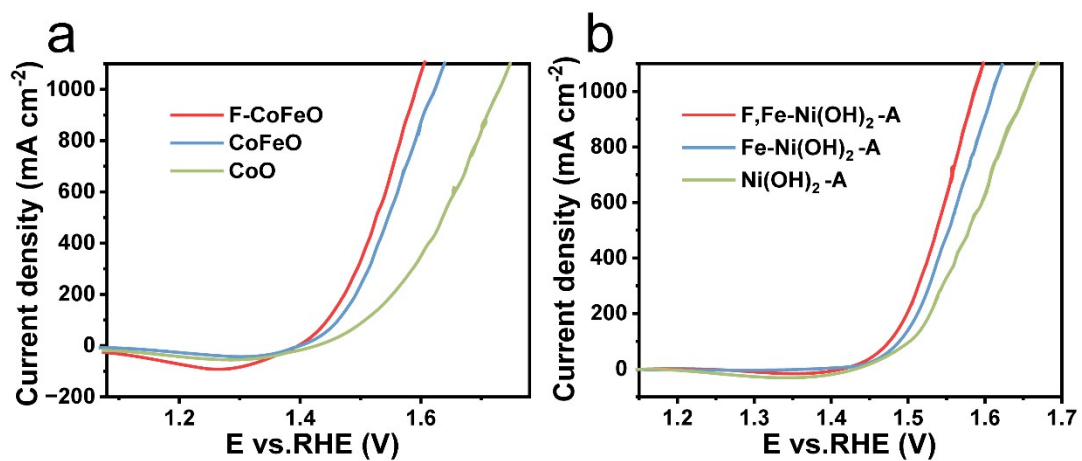
Fig. S27. RLSV curves with iR-compensation of (**a**) CoO, CoFeO and F-CoFeO; (**b**) Ni(OH)$_2$-A, Fe- Ni(OH)$_2$-A and F, Fe-Ni(OH)$_2$-A.
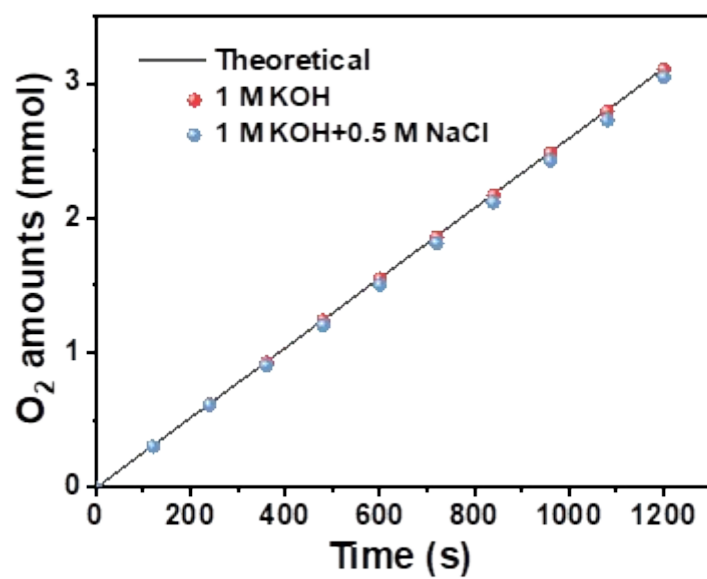
Fig. S28. The theoretical versus experimental O_2 evolved amounts recorded at current density of 1 A cm^{-2} in 1 M KOH and 1 M KOH + 0.5 M NaCl.
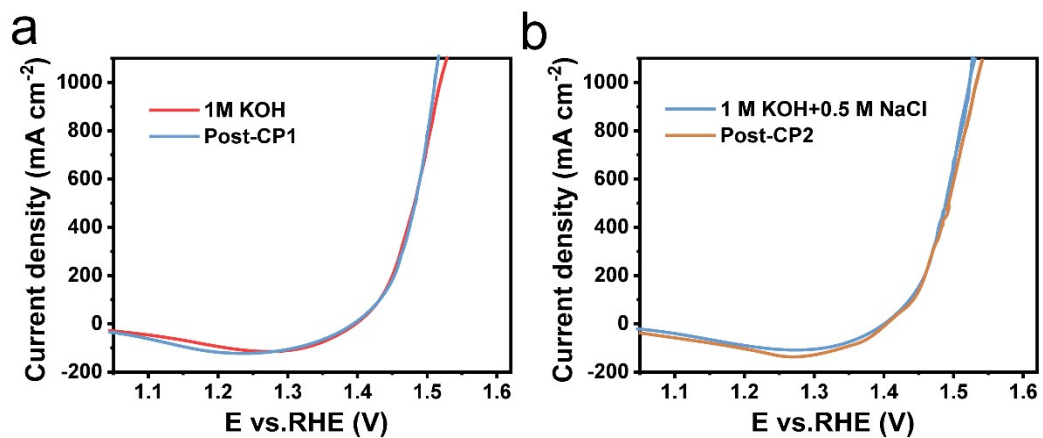
Fig. S29. Adsorption energy of *Cl and *OH on NiOOH, NiFeO$_2$ and F-NiFeO$_2$ surfaces.

Table S7. Overpotential comparisons with the most of recently reported electrocatalysts at large current densities in 1 M KOH.

| Catalysts	j (mA cm^{-2})	η (mV)	Ref.
F-NiFeO	**500**	**258**	**This**
	1000	**290**	**work**
NiFe-Boride	1000	460	[9]
NiFe-LDH	500	300	[10]
	1000	340	
NiFe(OH)$_x$/FeS/IF	500	304	[11]
	1000	332	
Fe-NiSOH	500	268	[12]
FeNi(MoO$_4$)$_x$	1000	351	[4]
Ni-Co-Se	500	279	[13]
	1000	329	
S-FeOOH/IF	500	324	[7]
	1000	358	
NiMoO$_x$/NiMoS	500	278	[14]
	1000	334	
Ni$_x$FeN/Ni$_3$N	500	288	[15]

Table S8. Overpotential comparisons with the most of recently reported electrocatalysts at different current densities in 1 M KOH+0.5 M NaCl.

Catalysts	j (mA cm^{-2})	η (mV)	Ref.
F-NiFeO	**100**	**208**	**This**
	500	**260**	**work**
	1000	**295**	
NiOOH@FeOOH	500	292	[16]
Ni$_3$S$_2$/Fe-NiP$_x$/NF	1000	310	[17]
Gly-NCP	100	268	[18]
NiPS/NF	100	329	[19]
	500	391	
NiFeSP	100	212	[20]
S-(Ni,Fe)OOH	100	278	[21]
	500	339	
	1000	378	

Fig. S30. (**a, b**) RLSV curves with iR-compensation before and after CP test in1 M KOH and 1 M KOH + 0.5 M NaCl. (F-NiFeO after CP test in 1M KOH and 1 M KOH + 0.5 M NaCl denoted as Post-CP1 and Post-CP2, respectively.)
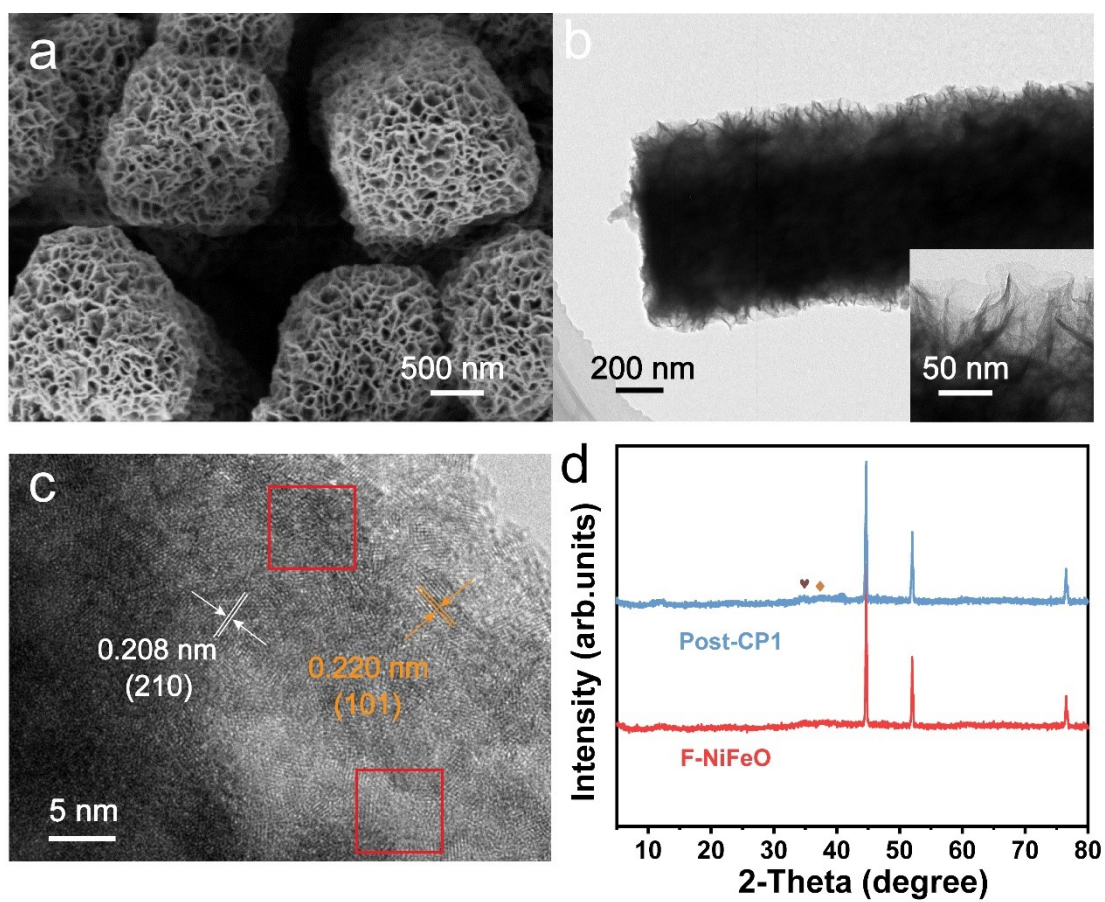
Fig. S31. (**a**) SEM image, (**b**)TEM image (the inset is TEM image with different magnification), (**c**) HRTEM image (the red boxes indicate the presence of lattice defects) and (**d**) XRD pattern of Post-CP1.
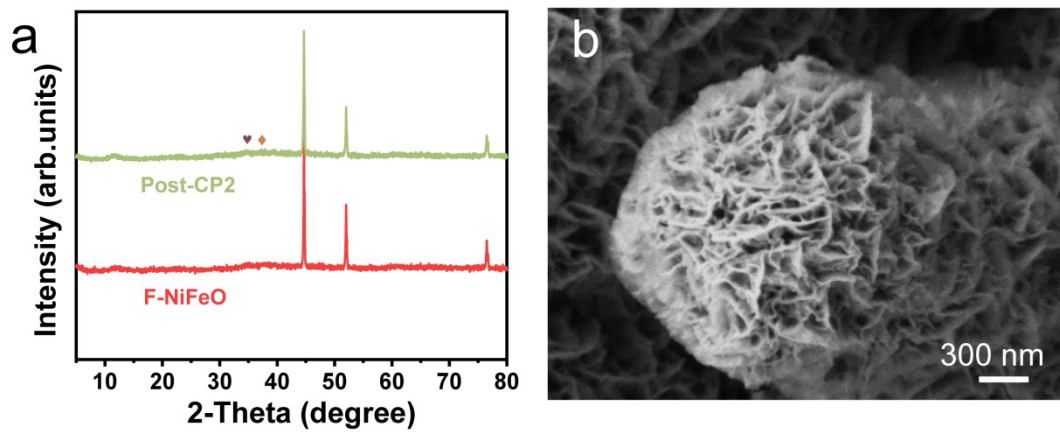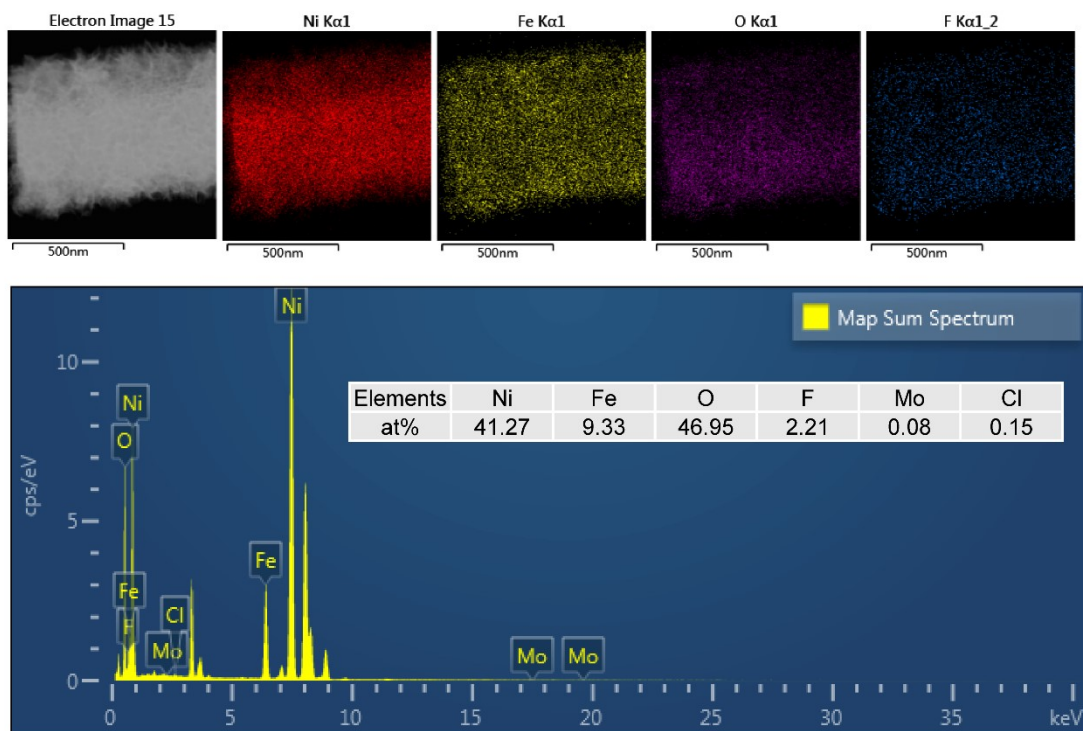
Fig. S32. (**a**) XRD pattern and (**b**)SEM image of Post-CP2.

Elements	Ni	Fe	O	F	Mo	Cl
at%	41.27	9.33	46.95	2.21	0.08	0.15

Fig. S33. Element mapping images and EDS of Post-CP1.
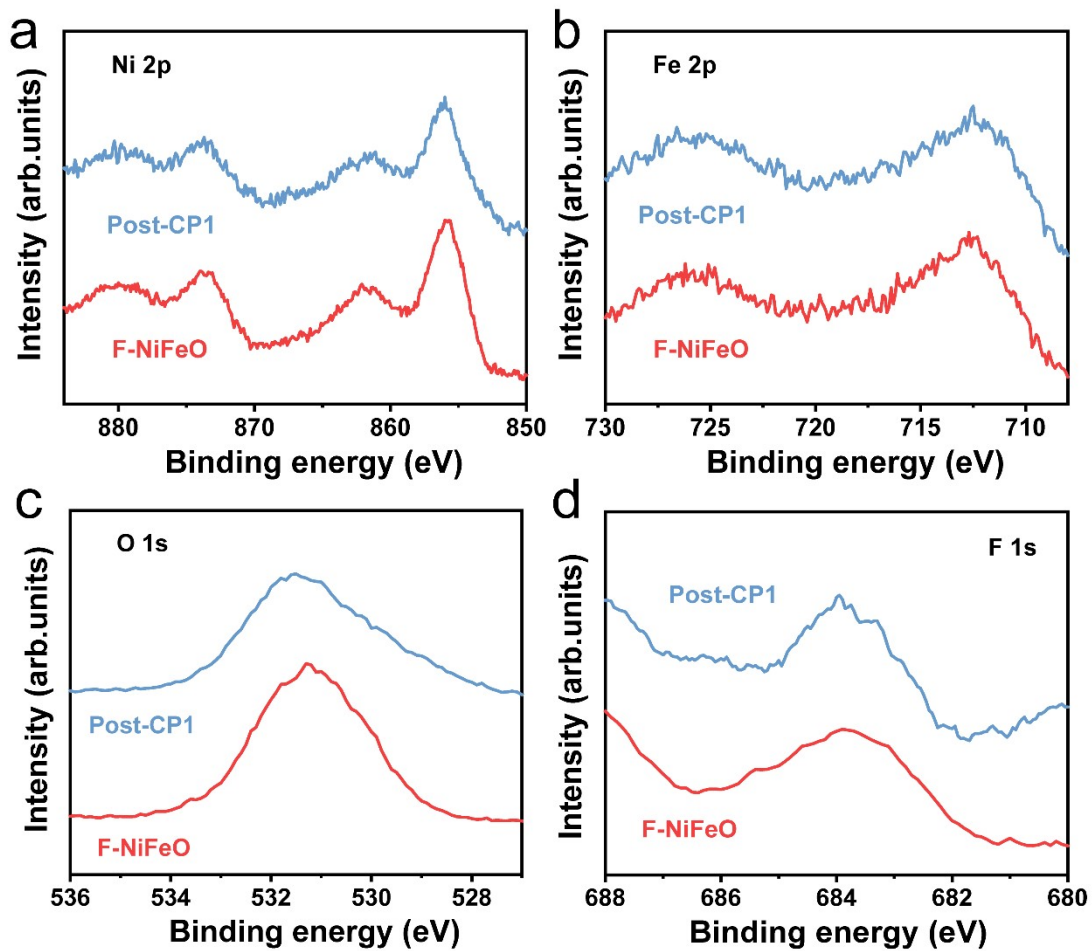
Fig. S34. (**a**) Ni 2p, (**b**) Fe 2p, (**c**) O 1s and (d) F 1s XPS spectra of Post-CP1.
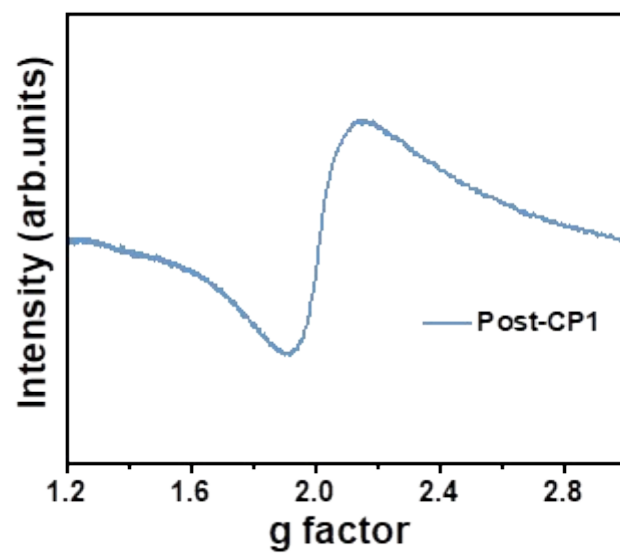
Fig. S35. EPR curve of Post-CP1.

Table S9. Quantitative analysis of different oxygen species of F-NiFeO and Post-CP1 based on the fitting result of O 1s XPS spectra.

(%)	O1	O2	O3
F-NiFeO	25.73	40.27	34.00
Post-CP1	30.63	38.58	30.79

Table S10. Element content in electrolyte (1M KOH) detected by ICP-OES.

Electrolyte	Ni (ppm)	Fe (ppm)
After CV	<0.001	0.027
After-CP	<0.001	0.021

Ni and Fe contents were measured in electrolyte after electrochemical activation (denoted as After-CV) and the electrolyte after 100 h CP testing (denoted as After-CP). It can be found that Ni is almost not dissolved and Fe content in the electrolyte almost unchanged, which is because the OER process involves the equilibration of dynamic dissolution and redeposition of Fe to maintain the stability of the catalyst.[22]

a

b
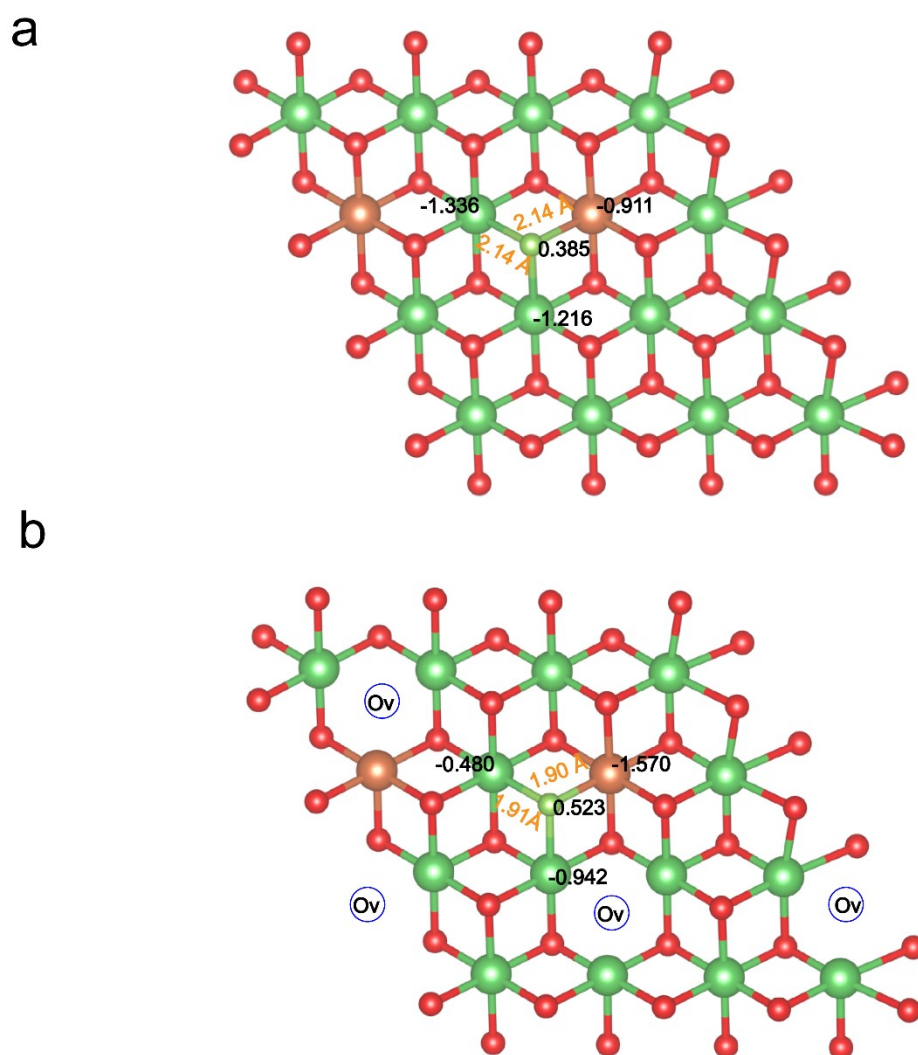
Fig. S36. Computed Bader charges in (**a**) F-NiFeO$_2$ without O$_{vac}$ and (**b**) F-NiFeO$_2$ with O$_{vac}$ models.
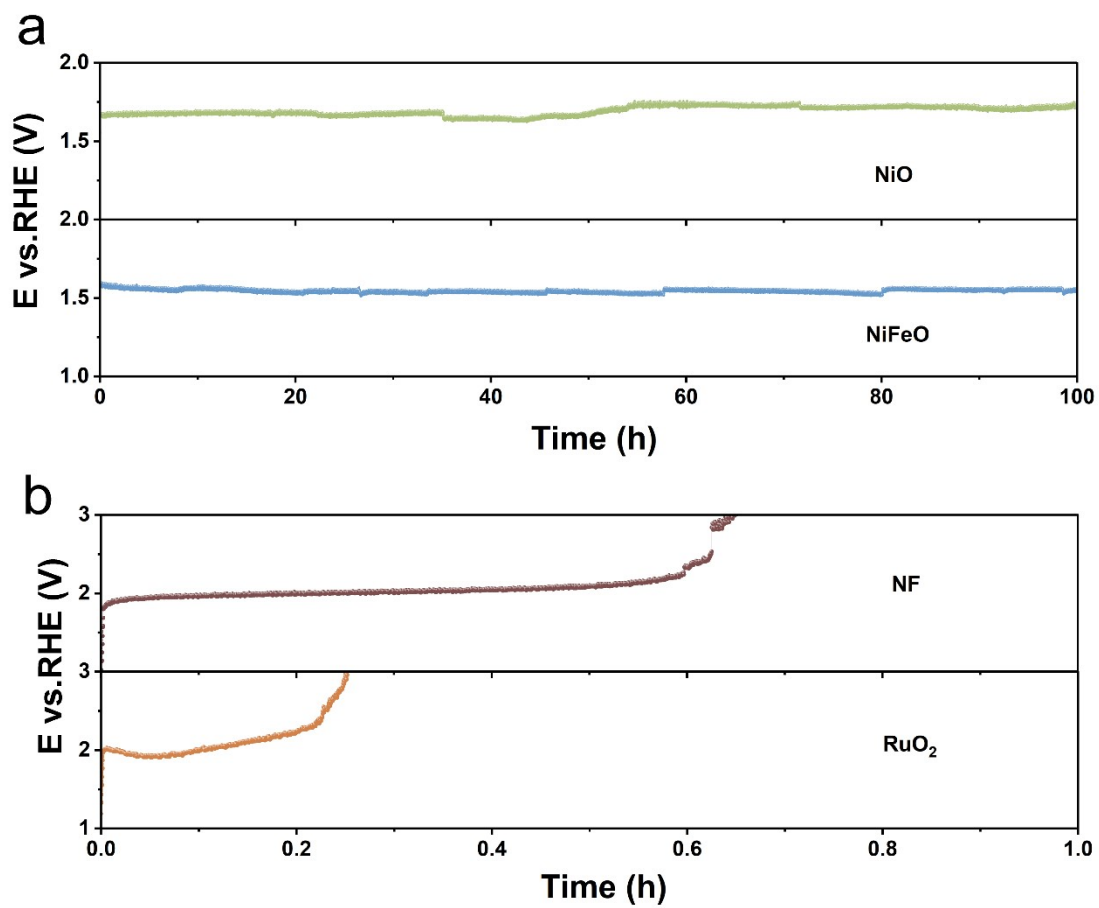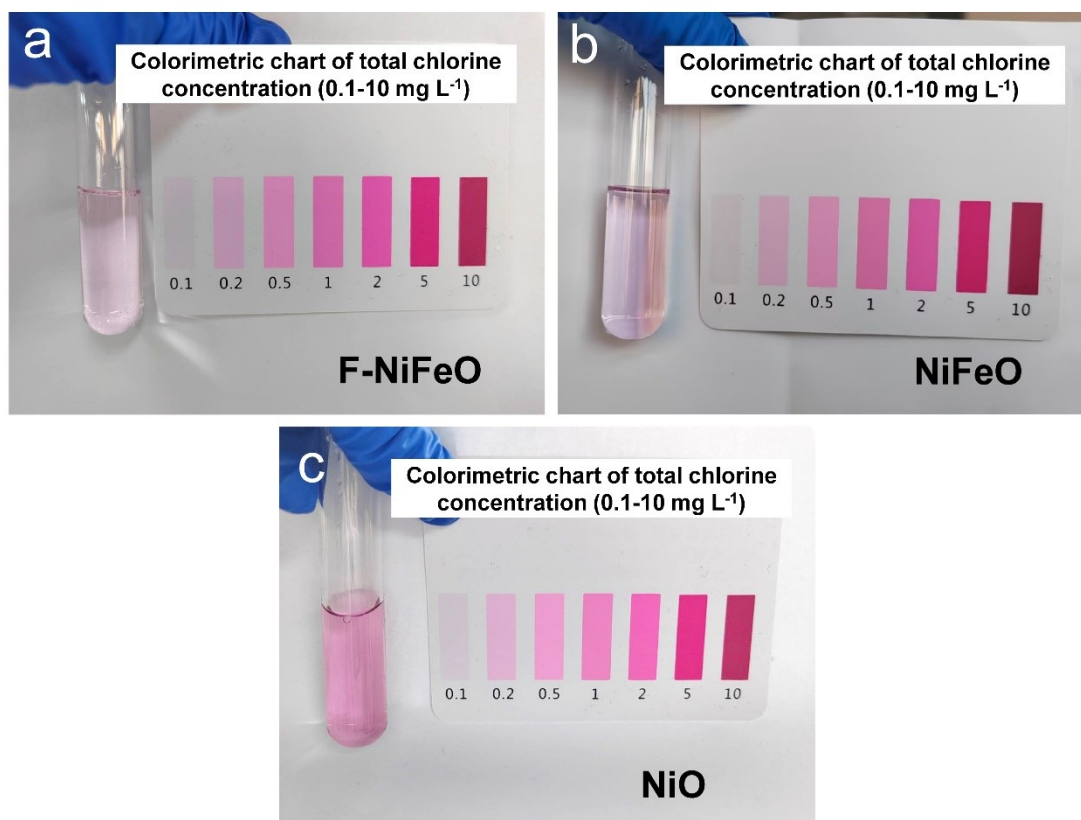
Fig. S37. (**a, b**) CP curves with iR-compensation of NiFeO, NiO, RuO$_2$ and NF at a constant current density of 1 A cm^{-2} in 1 M KOH + 0.5 M NaCl.
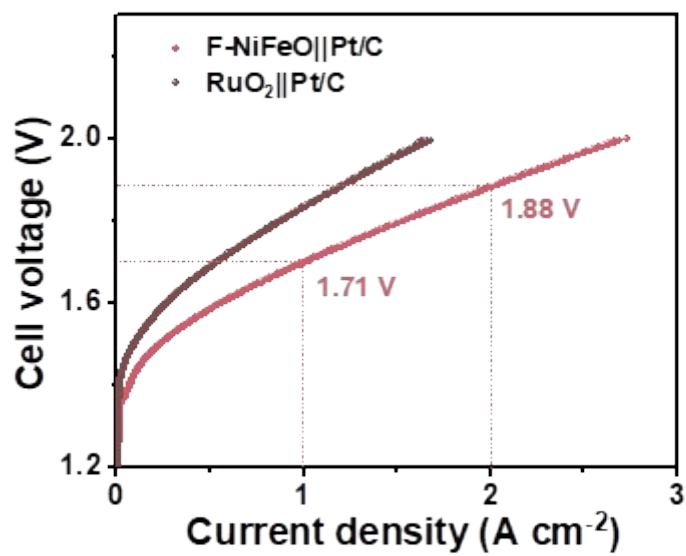
Fig. S38. ClO$^-$ detection of (a)F-NiFeO, (b)NiFeO and (c)NiO after 100h CP test in 1 M KOH + 0.5 M NaCl.
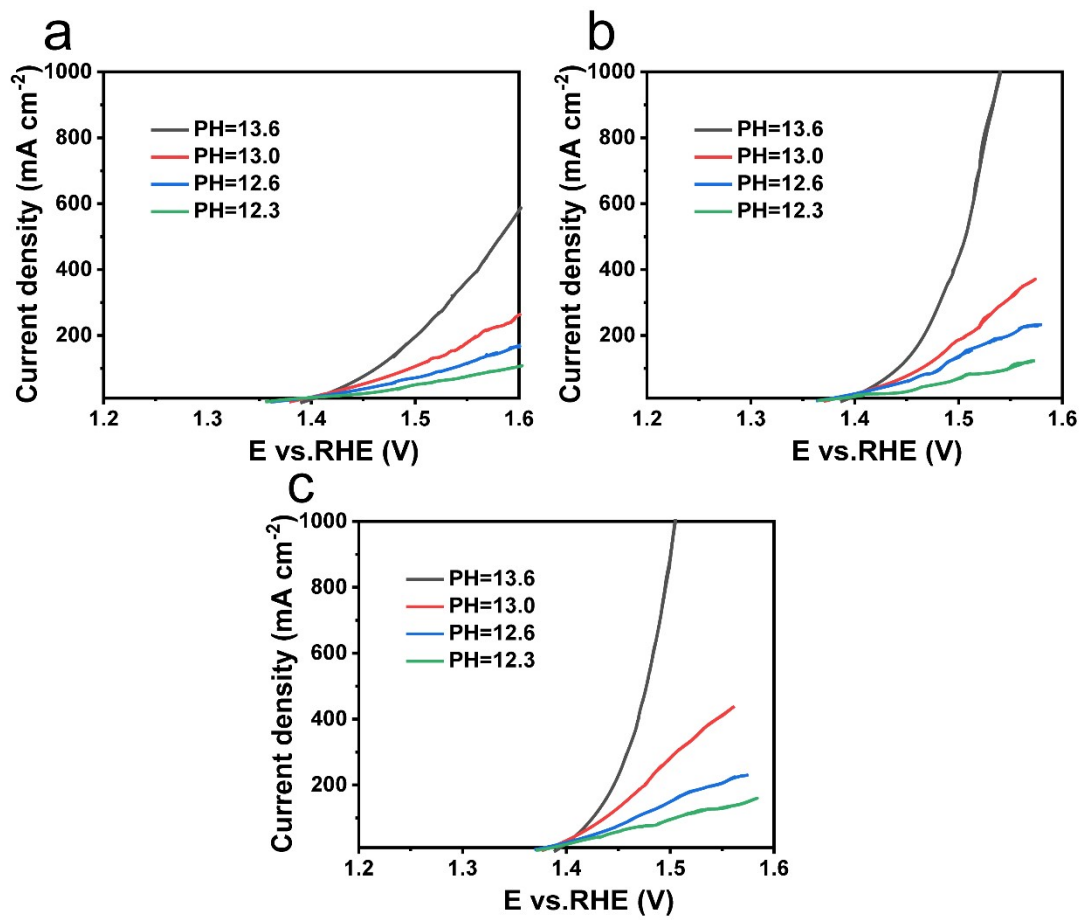
The ClO$^-$ generated in the electrolytes was detected by a colorimetric method. Compared to NiFeO and NiO, only a very small amount of ClO$^-$ is formed for F-NiFeO, indicating its optimal OER selectivity.
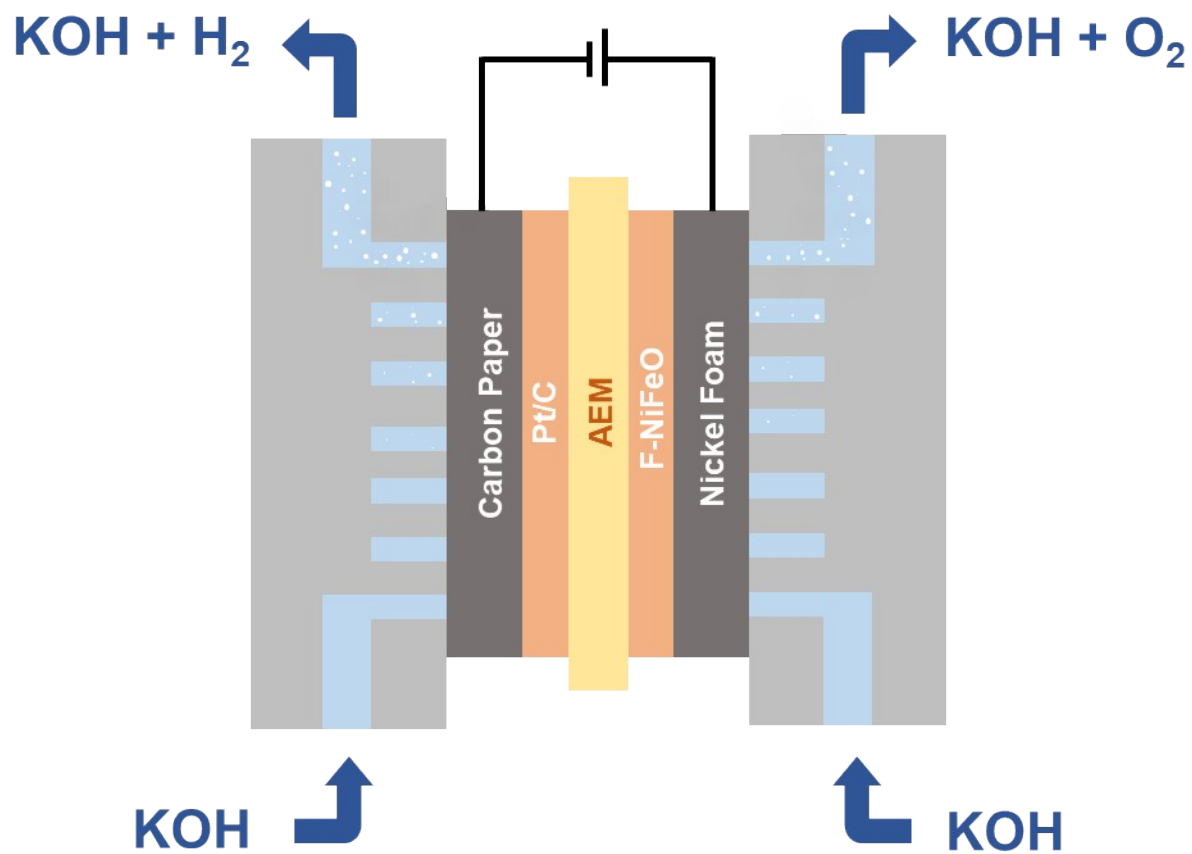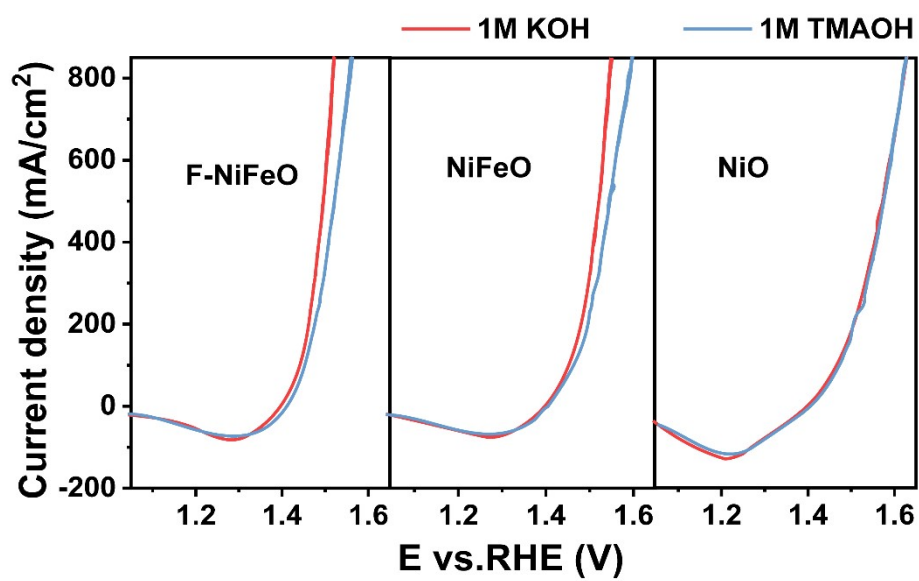
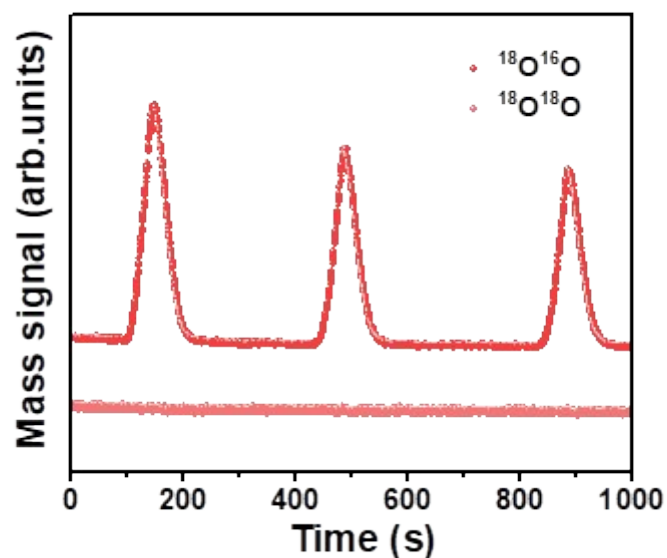**Fig. S39**. Schematic diagram of AEM electrolyzer.

Fig. S40. LSV curves in AEM electrolyzer (1 M KOH, 70 ℃).

**Fig. S41**. PH dependence LSV polarization curves of (**a**) NiO, (**b**) NiFeO and (**c**) F-NiFeO.

**Fig. S42**. RLSV curves for NiO, NiFeO and F-NiFeO measured in 1 M KOH and 1 M TMAOH.

Fig. S43. The DEMS signals of $^{34}O_2$ and $^{36}O_2$ vs. time for F-NiFeO.

As the lattice oxygen (^{18}O) is consumed, the oxygen in the electrolyte (^{16}O) will be replenished to the electrode and converted into lattice oxygen, resulting in a gradual weakening of the $^{18}O^{16}O$ signal. However, the amount of ^{18}O exchanged into the electrolyte in the electrode is very small, so it is difficult to detect O_2 from the combination of ^{18}O in the electrolyte and lattice ^{18}O.
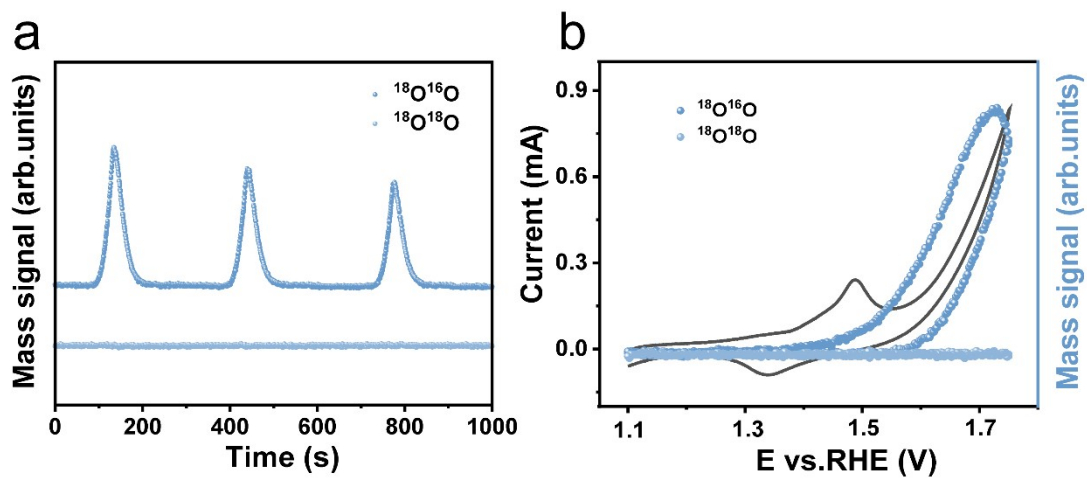
Fig. S44. (**a**) The DEMS signals of $^{34}O_2$ and $^{36}O_2$ vs. time for NiFeO. (**b**) The DEMS signals of $^{34}O_2$ and $^{36}O_2$ *vs.* applied potential for NiFeO.
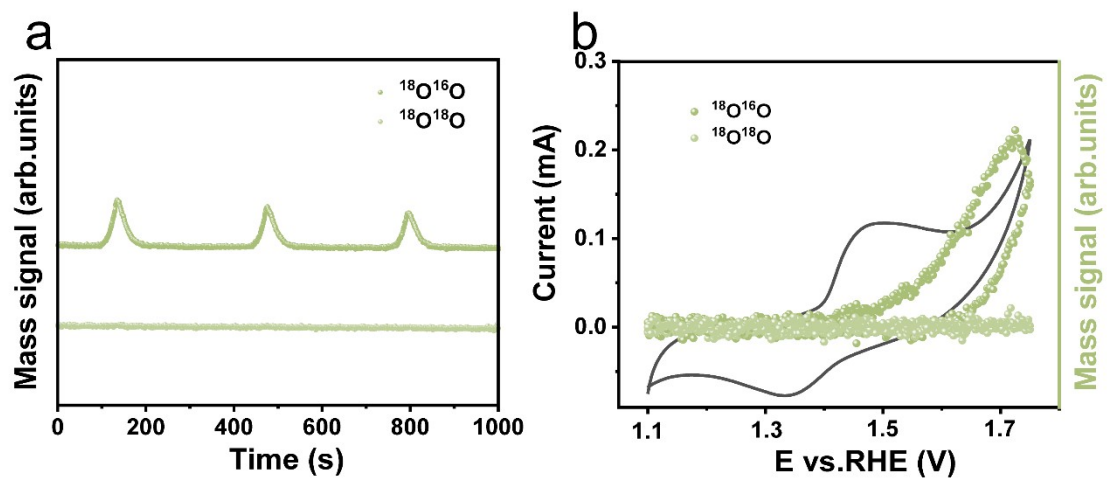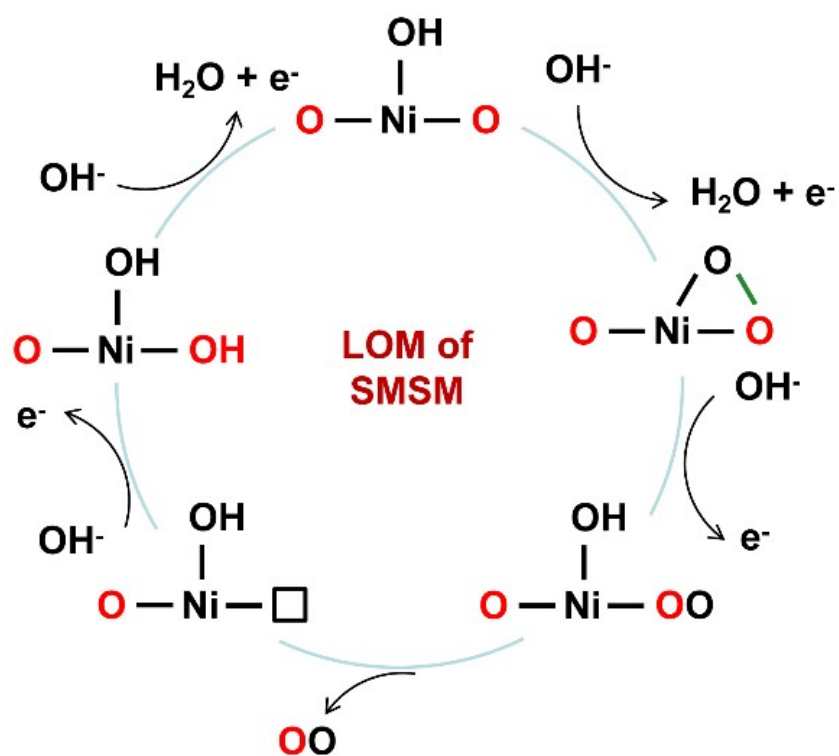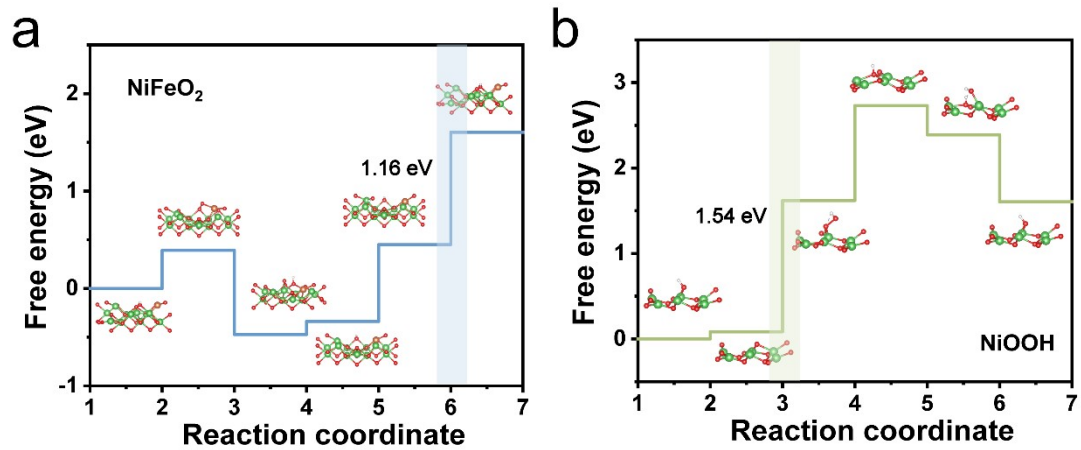
Fig. S45. (**a**) The DEMS signals of $^{34}O_2$ and $^{36}O_2$ vs. time for NiO. (**b**) The DEMS signals of $^{34}O_2$ and $^{36}O_2$ *vs.* applied potential for NiO.

Fig. S46. Schematic illustration of LOM of SMSM pathway.

Fig. S47. Gibbs free energy diagrams in (a) NiFeO$_2$ and (b) NiOOH models (Ni, Fe and O are shown in green, yellow and red, respectively).

References

1. C. Wang, P. Zhai, M. Xia, W. Liu, J. Gao, L. Sun and J. Hou, *Adv. Mater.*, 2023, **35**, 2209307.

2. Z. Cai, P. Wang, J. Zhang, A. Chen, J. Zhang, Y. Yan and X. Wang, *Adv. Mater.*, 2022, **34**, 2110696.

3. N. Zhang, X. Feng, D. Rao, X. Deng, L. Cai, B. Qiu, R. Long, Y. Xiong, Y. Lu and Y. Chai, *Nat. Commun.*, 2020, **11**, 4066.

4. K. Dastafkan, S. Wang, C. Rong, Q. Meyer, Y. Li, Q. Zhang and C. Zhao, *Adv. Funct. Mater.*, 2022, **32**, 2107342.

5. X. Zhang, Y. Li, Z. Wu, H. Sheng, Y. Hu, C. Li, H. Li, L. Cao and B. Dong, *Mater. Today Energy*, 2022, **26**, 100987.

6. Q. Xu, H. Jiang, X. Duan, Z. Jiang, Y. Hu, S. W. Boettcher, W. Zhang, S. Guo and C. Li, *Nano Lett.*, 2021, **21**, 492-499.

7. X.-Y. Zhang, F.-T. Li, Y.-W. Dong, B. Dong, F.-N. Dai, C.-G. Liu and Y.-M. Chai, *Appl. Catal., B*, 2022, **315**, 121571.

8. Y. Li, Y. Wu, M. Yuan, H. Hao, Z. Lv, L. Xu and B. Wei, *Appl. Catal., B*, 2022, **318**, 121825.

9. N. Wang, A. Xu, P. Ou, S.-F. Hung, A. Ozden, Y.-R. Lu, J. Abed, Z. Wang, Y. Yan, M.-J. Sun, Y. Xia, M. Han, J. Han, K. Yao, F.-Y. Wu, P.-H. Chen, A. Vomiero, A. Seifitokaldani, X. Sun, D. Sinton, Y. Liu, E. H. Sargent and H. Liang, *Nat. Commun.*, 2021, **12**, 6089.

10. Y. P. Liu, X. Liang, L. Gu, Y. Zhang, G. D. Li, X. X. Zou and J. S. Chen, *Nat. Commun.*, 2018, **9**, 2609-2619.

11. S. Niu, W. J. Jiang, T. Tang, L. P. Yuan, H. Luo and J. S. Hu, *Adv. Funct. Mater.*, 2019, **29**, 1902180-1902189.

12. C. Huang, Q. Zhou, D. Duan, L. Yu, W. Zhang, Z. Wang, J. Liu, B. Peng, P. An, J. Zhang, L. Li, J. Yu and Y. Yu, *Energy Environ. Sci.*, 2022, **15**, 4647-4658.

13. J. Abed, S. Ahmadi, L. Laverdure, A. Abdellah, C. P. O'Brien, K. Cole, P. Sobrinho, D. Sinton, D. Higgins, N. J. Mosey, S. J. Thorpe and E. H. Sargent, *Adv. Mater.*, 2021, **33**, 2103812.

14. P. Zhai, Y. Zhang, Y. Wu, J. Gao, B. Zhang, S. Cao, Y. Zhang, Z. Li, L. Sun and J. Hou, *Nat. Commun.*, 2020, **11**, 5462.

15. F. Cai, L. Liao, Y. Zhao, D. Li, J. Zeng, F. Yu and H. Zhou, *J. Mater. Chem. A*, 2021, **9**, 10199-10207.

16. B. Wu, S. Gong, Y. Lin, T. Li, A. Chen, M. Zhao, Q. Zhang and L. Chen, *Adv. Mater.*, 2022, **34**, 2108619.

17. X. Luo, P. Ji, P. Wang, X. Tan, L. Chen and S. Mu, *Adv. Sci.*, 2022, **9**, 2104846.

18. Z. Song, K. Wang, Q. Sun, L. Zhang, J. Li, D. Li, P.-W. Sze, Y. Liang, X. Sun, X.-Z. Fu and J.-L. Luo, *Adv. Sci.*, 2021, **8**, 2100498.

19. H.-Y. Wang, J.-T. Ren, L. Wang, M.-L. Sun, H.-M. Yang, X.-W. Lv and Z.-Y. Yuan, *J. Energy Chem.*, 2022, **75**, 66-73.

20. Y. Wu, Y. Zhao, P. Zhai, C. Wang, J. Gao, L. Sun and J. Hou, *Adv. Mater.*, 2022, **34**, 2202523.

21. L. Yu, L. Wu, B. McElhenny, S. Song, D. Luo, F. Zhang, Y. Yu, S. Chen and Z. Ren, *Energy Environ. Sci.*, 2020, **13**, 3439-3446.

22. Q. Zhang, W. Xiao, H. C. Fu, X. L. Li, J. L. Lei, H. Q. Luo and N. B. Li, *ACS Catal.*, 2023, **13**, 14975-14986.